Eindhoven University of Technology

MASTER

Observations of excited (bi)exciton and multi-exciton features in locally homogeneous quantum dots

van Lippen, T.

Award date:
2002

TU/e technische universiteit eindhoven

Department of Applied Physics
Semiconductor Physics

Observations of Excited (Bi)Exciton and Multi-Exciton Features in Locally Homogeneous Quantum Dots

Twan van Lippen
August 2002

Supervisors: Ir. F.P.J. de Groote
Dr. J.E.M. Haverkort

Graduation Professor: Prof. dr. J.H. Wolter

HGF

Abstract

In ensembles of self-assembled quantum dots (QDs), inhomogeneous broadening effects tend to partially obscure the multi-excitonic features. In this study we investigate locally homogeneous, strain-free GaAs QD-arrays by micro-photoluminescence (μ-PL) at low temperature. The spectra indicate that the QDs exhibit excellent homogeneity on length scales up to several microns. The PL linewidth of the homogeneous QD-arrays has been shown to be as narrow as 170 μeV, allowing to clearly resolve multi-excitonic features. Using a Hartree-Fock (HF) based calculations including Coulomb and exchange energies, the observed spectra can be assigned to excitonic and multi-excitonic transitions, including excited single exciton and excited biexciton transitions. The strong excited excitonic features are explained by incomplete carrier relaxation pointing toward the presence of a phonon bottleneck. Two fitting methods based on HF-approximations are able to explain the regularity of the positions of the peaks in the measured PL spectra. It is shown that the fitting methods predict the observed PL peaks quite well and that the extracted Coulomb and exchange values also show a good agreement with theoretical calculated values.

Contents

Chapter 1

Introduction

1.1 General Introduction

Semiconductor quantum dots (QDs) are often described as artificial atoms due to their δ-function-like density of states. This analogy is nicely reflected in the fact that both free atoms and QDs exhibit optical line spectra with narrow linewidth. However, in optical spectroscopy of QDs the observed linewidths are orders of magnitude broader compared to atoms. In semiconductor QDs, lower band gap material with typical lateral dimensions of 1 - 40 nm, corresponding to about 10^3 - 10^7 lattice atoms are embedded into a matrix of higher band gap material. Due to complete size quantisation of the electronic levels in the QD, the associated density of state is discrete. However, because of the discrete energy spectrum, the carrier relaxation dynamics in QDs are significantly different from those in systems with continuous spectra.

In structures with higher dimensionality such as quantum wells and wires the density of states is still continuous in translationary invariant directions. The optical absorption is therefore continuous as well, with a cutoff at the effective band gap of the material. The optical emission appears at or slightly below the energy of the band gap. The situation in QDs is not so different, except that lateral motion in the vicinity of the QD is quantised. Assuming fast relaxation almost all excitons will end up in the ground state of the QD prior to radiative recombination. Optical excitation of a single QD does therefore result in a narrow emission line at the position of the ground state energy. The excitonic ground state is a well-defined quantity in a QD, it is a stationary eigenvalue in a confined environment. The impressive progress in the fabrication of low-dimensional semiconductor structures during the last two decades made it possible to reduce the effective dimensionality from three dimensional bulk materials to quasi-zero dimensional quantum dots. This was due to the fact that the QD properties are, to a certain degree, controllable by the flexibility in the structure design and the subsequent growth process. Nucleation and crystal growth however, happen not strictly in thermodynamic equilibrium but also involve kinetic processes. Therefore, size fluctuations will occur during the formation of QDs. In the next paragraph, a brief introduction in the mechanism of quantum dot growth is given.

1.2 Growth of Quantum Dots

Several methods of producing quantum dots are available. The vast majority of quantum dots are produced by a technique which uses epitaxial growth. One of the best candidates for the study of single quantum dots are the self-assembled quantum dots formed by the Stranski-Krastanov growth principle. Those are created by a thermodynamic instability during the two-dimensional growth of layers with different lattice constants. A layer with a lower energy band gap and a certain lattice constant, for example InAs, is grown on top of a layer with a higher energy band gap and a different lattice constant, for example GaAs. For thin InAs layers below a critical thickness, first a pseudomorphic layer with the lateral lattice constant of underlying (GaAs) layer is formed, see Fig. 1.1. With increasing InAs layer thickness the accumulated compressive strain can no longer be accommodated in a two-dimensional arrangement. The system will get unstable against the formation of three-dimensional, coherently strained islands with reduced strain energy but enhanced surface energy. This process leads to the formation of approximately equally-sized, dislocation-free InAs islands, so-called self-assembled QDs (SAQDs).

They are arranged on top of the remaining part of the two-dimensional InAs layer, the so-called wetting layer. Individual QDs nucleate typically in disordered arrays with nearest-neighbor separations down to 30 nm, corresponding to QD surface density up to about 10^{11} cm^{-2}. Figure 1.2 shows an Atomic Force Microscopy (AFM) image and a cross-sectional Scanning Tunnelling Microscopy (X-STM) current image of SAQDs. By capping these self-assembled islands with an epitaxial layer, similar to that of the substrate, high quality QDs can be produced. A typical PL spectrum from an ensemble of SAQDs is shown in Fig. 1.3, resulting in a inhomogeneously broadened PL peak due to size fluctuations.

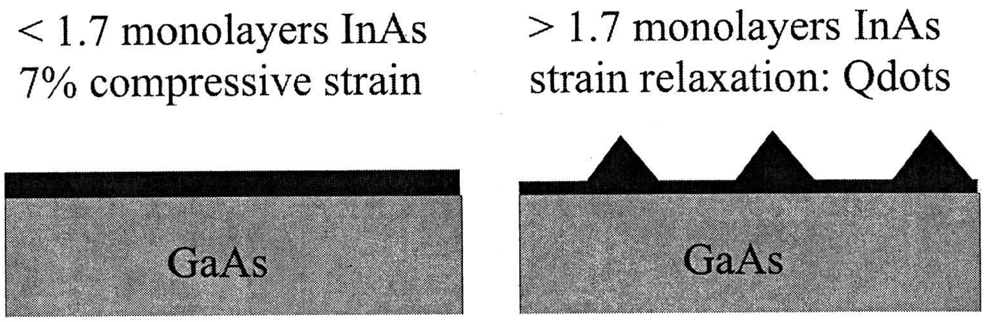

Figure 1.1: *Formation of InAs SAQDs via the Stranski-Krastanov growth principle.*

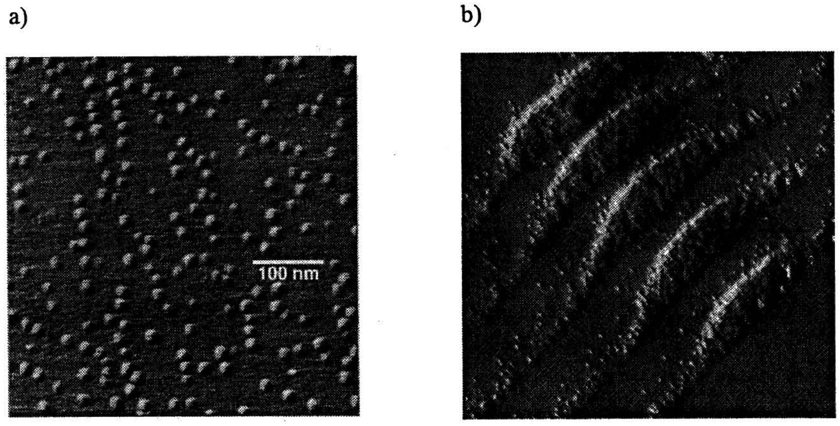

Figure 1.2: *a) AFM image of uncapped InAs GaAs SAQD, showing a random dot distribution over the sample surface [1]. b) X-STM current image of D. Bruls et al. [2] on stacked quantum dots.*

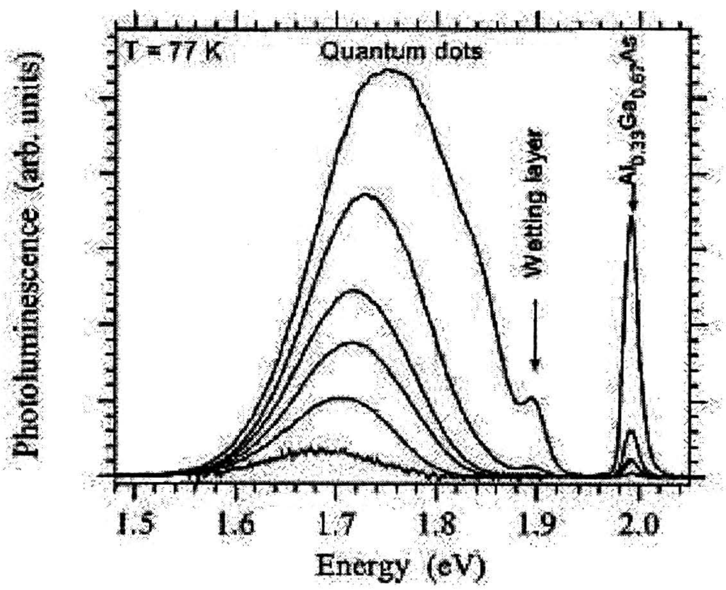

Figure 1.3: *PL spectra of an ensemble of SAQDs for a broad range of excitation densities [3].*

1.3 Motivation and Outline of report

As said before, the transition energies of QDs are determined by size quantisation. The ability to clearly understand and unambiguously interpret the experimental results have been limited for some time by the inhomogeneous broadening of the observed PL peaks. Thus, it is important to establish techniques to detect the PL from a single quantum dot in order to clarify its nature. A possible way to get access to a single QD in real space in general is etching mesa structures in a QD sample. Also covering the QD sample with a mask consisting of small (submicrometer-size) holes is a commonly used technique. Confocal PL microscopy, which allows us to obtain spatial resolutions in the range of 1 μm is also an option. Another way to achieve access to a single QD spectrum in real space is connected to sample preparation. Low density ensembles of homogeneous QDs can be obtained by special growth conditions. Using growth on patterned substrates, QDs on predefined positions are even introduced [4].
The first observations of narrow emission lines from QDs were reported about ten years ago. The work in that stage was concerned primarily with the demonstration of theoretical predicted sharp PL peaks of single QDs. Spatially resolved investigations have been performed on QDs using confocal microscopy [5]. Experiments showed an optical linewidth of the order of 100 μeV. Thus, by probing micron-size lateral region of QDs samples, it was found that the inhomogeneously broadened spectra resolved into a sharp peaks which corresponds to the recombination of excitons bound in QDs, see Fig. 1.4. In those early stages, properties of QDs considering the ground state have been investigated in the one exciton limit. Again the analogy with atoms can be made, one exciton is commonly described as being hydrogen atom, the biexciton can be described as helium atoms and lithium is the analogue for three excitons. Of importance for fundamental research are spectroscopic results in the few exciton limit. Multi-excitonic complexes in QDs also attract the attention from researchers because of their application of QDs for photonic switching due to the large non-linearity of multi-excitonic complexes. Clear signatures of the biexciton state in single QDs have been obtained by power dependent PL [7, 6]. Higher exciton occupancies leave a more and more complicated fingerprint in the emission spectra of single QDs [8].
The appereance of biexciton and multi-exciton spectrum is heavily influenced by the carrier relaxation dynamics. Carrier relaxation from excited dot energy levels to energetically lower dot energy levels can already be hindered at low excitation densities (Pauli blocking).

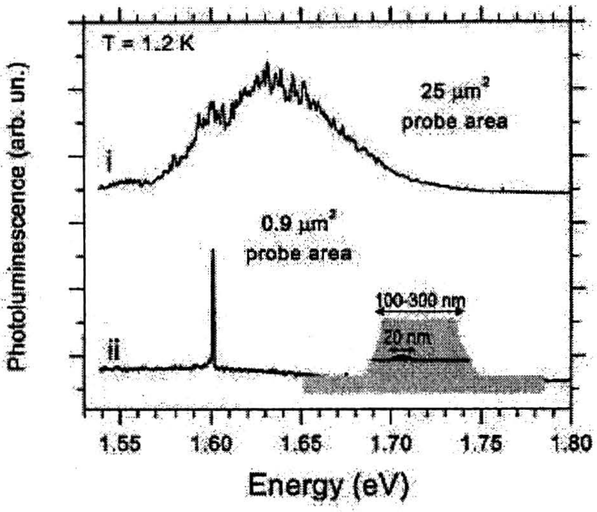

Figure 1.4: *PL showing emission from SAQDs when probing (i) an ensemble of ~ 100 SAQDs and (ii) a single QD. The schematic drawing shows a schematic overview of the measured sample [3].*

Observations of excited single and biexciton complexes, pointing towards the presence of a phonon bottleneck have been shown by measurements. Many body interactions [9, 10, 11] and spin related relaxation phenomena [12] also complicate PL spectra from single QDs as will be seen in this report.

Our goal to study the fundamental physics of QDs requires an as simple as possible QD system. We therefore want to avoid the smearing out of optical and electrical properties of QDs and study the sought-for zero dimensional behavior. To be able to do so, a sample with uniform QD-arrays on predefined positions is used, grown by Nötzel *et al.* by a technique that combines both elements of self-organisation and patterning. The advantage of this sample is the high size uniformity of the QDs along the array. Even by exciting a number of QDs, one single sharp PL peak is observed indicating a homogeneous size distribution of the QDs. The special sample configuration together with the use of confocal PL microscopy allows us to study the intrinsic properties of only a small number of identical QDs avoiding the smearing out of QDs properties due to the size distribution of the QDs. The QDs under investigation (i) are strain free (ii) exhibit no electrical field due to piezo electric effects (iii) are non-degenerate and (iv) have a high confinement for the carriers and therefore we consider our QDs as "ideal" QDs. Most investigations have been performed on SAQDs, which do not exhibit these criteria of an ideal QD. Hence fast relaxation of carriers is observed in SAQDs [27], however in our case of an ideal QD, slowed relaxation pointing toward a phonon bottleneck is more likely to be present. In this report, we hope to overcome some of the obstacles by studying single dots of an ensemble of self assembled QDs by various PL measurements. The measurements show complicated PL spectra with various sharp lines. By carrying out detailed analysis of the PL spectra we hope to find an appropriate model to explain PL line(s) in the emission spectra of QDs and ultimately be able to predict various PL line(s).

In chapter 2 some intrinsic properties of QDs, which will be important in the remainder of this report will be addressed. The relevant theoretical concepts are outlined and special attention is given to the quantum mechanics of the carriers in the QDs.

The various experimental techniques and equipment used for this work is explained in chapter 3. The sample structure and characteristics are summarised. The installation of the monochromator is discussed and subsequently the micro-photoluminescence setup is described. The basics of the PL technique is given ending with possible variations on the PL technique.

In chapter 4, the PL measurements are carried out and discussed. First a brief overview is given of previous results of PL on QDs. The experimental observations are shown and conclusions concerning QD homogeneity are drawn. Next the interpretation of the observed spectra is analysed and subsequently the analysis is discussed.

Finally, conclusions and recommendations are given in chapter 5.

Chapter 2

Theoretical Concepts

2.1 Introduction

Much experimental and theoretical effort has been performed in realisation and study of low-dimensional semiconductor structures. The engineering and understanding of materials at nanometer scale is a challenging subject. New effects, for instance due to quantum mechanics, have been discovered in such nanostructures. Reduced dimensionality and hence the discrete density of states of QDs leads to new physical properties. Also the filling of the QDs with multiple excitons requires a many-body approach to describe the phenomena in the QD [9, 10, 11]. Furthermore, the carrier relaxation dynamics in QDs is a topic of discussion and is a key issue concerning the filling of QDs. This chapter is concerned with the theoretical aspects of the relevant phenomena in nanoscaled structures.

2.2 Towards Quantum Dots

2.2.1 Dimensionality in Semiconductors

In a bulk semiconductor, the carriers are free to move, so their energy spectrum is continuous. The density of states per unit energy increases as the square-root of energy, see Fig. 2.1. Two things will happen when a particle is confined to a small volume in space: the particle acquires kinetic (referred to as confinement) energy, and the energy spectrum becomes discrete [14]. The reduction of dimensionality is directly reflected in the dependence of the density of states on energy, see Fig. 2.1.

The density of states for a three dimensional system (bulk semiconductor) has the form

$$\frac{dN}{dE} \propto \frac{d}{dE}E^{3/2} = E^{1/2}. \tag{2.1}$$

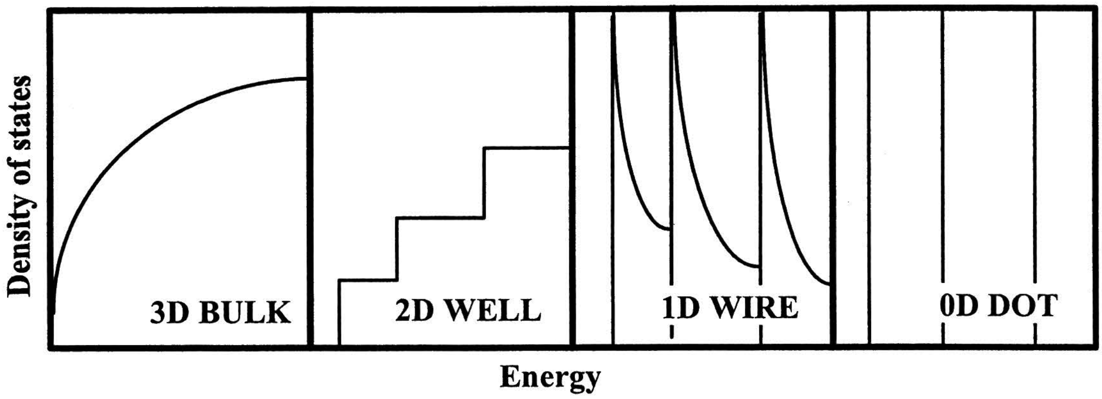

Figure 2.1: *Density of states as a function of energy in systems with different numbers of spatial dimensions: 3D, bulkmaterial; 2D, quantum well; 1D, quantum wire; 0D, quantum dot. Typical intraband level spacings in QDs (ground to first excited states) are in the range of 10 to 100 meV, see 2.3.1.*

For a two-dimensional system (quantum well) the density of states is a step function,

$$\frac{dN}{dE} \propto \frac{d}{dE}\sum_{\epsilon_i<E}(E-\epsilon_i) = \sum_{\epsilon_i<E} 1; \tag{2.2}$$

for a one-dimensional system (quantum wire)the density of states has a discontinuity,

$$\frac{dN}{dE} \propto \frac{d}{dE}\sum_{\epsilon_i<E}(E-\epsilon_i)^{1/2} = \sum_{\epsilon_i<E}(E-\epsilon_i)^{-1/2}; \tag{2.3}$$

and for a zero-dimensional system (quantum dot) the density of states has the shape of δ-peaks,

$$\frac{dN}{dE} \propto \frac{d}{dE}\sum_{\epsilon_i<E}\Theta(E-\epsilon_i)^{1/2} = \sum_{\epsilon_i<E}\delta(E-\epsilon_i). \tag{2.4}$$

Where ϵ_i are discrete energy levels, Θ is the Heaviside step function and δ is the Dirac function. The discrete energy spectrum in quantum dots gives rise to a strongly peaked density of states, which can lead to fundamentally different properties with respect to bulk or 2-D semiconductor structures. Strongly enhanced oscillator strengths and optical non-linearities are predicted as well as reduced relaxation of carriers.

2.2.2 Confinement Regimes

There are several different scales where you can think of for defining the confinement of the carriers. A generally used scale for defining the confinement is a length scale based on the Bohr radius of the bound state of an electron-hole pair and is defined as:

$$a_B = \varepsilon_r \frac{m_0}{m^*_{red}} a_{0,hydrogen}, \tag{2.5}$$

where m^*_{red} is the reduced effective mass of the electron-hole pair; ε_r is the relative permittivity and $a_{0,hydrogen} = 0.529$ Å. The Bohr radii of the exciton in GaAs dots is approximately 116 Å. Such a bound state of an electron and hole is called exciton and is analogous to a hydrogen atom. Even in a QD, when the charge carriers are bound by the confining potential rather than the Coulomb interaction, the electron-hole pair is still referred to as an exciton.

Three regimes of quantum confinement were introduced by Efros and Efros [13] depending on the Bohr radius of the electrons, holes and electron-hole pair respectively for spherical semiconductor QDs. The different confinement limits depend on whether the exciton Bohr radius of the exciton a_X is larger (strong confinement), smaller (weak confinement)than or equal (intermediate confinement) to the lateral dimensions of the QD. Comparing the lateral dimensions of the QD (40 nm) to the exciton Bohr radius, the exciton Bohr radius is much smaller. Hence the exciton is confined weakly by the QD dimensions. Another confinement scale, based on the ratio of the confinement energy of the carriers and the band gap energy offset, indicates strong confinement of the carriers, see 3.2.

2.3 Quantum Mechanical Approach

2.3.1 Particle in a Three-Dimensional Box

As said before, electrons can be confined in all three dimensions. In general it is impossible to obtain an analytical solution of the Schrödinger equation, but a simple model will illustrate the general physics. Such a simple model is justified since the band offsets, see

3.2 are relatively large. It should be mentioned that this model is only valid for a single particle confined in a volume. Let's consider a particle in a box of dimensions a, b and c in the x, y and z directions, respectively. The potential inside the box will be taken zero and outside the box the potential is set to infinity. The Schrödinger equation in the envelope aprroximation for a three-dimensional quantum box can be written as follow:

$$\Big\{-\frac{\hbar^2}{2m^*}\nabla^2 + V(x,y,z)\Big\}\psi(x,y,z) = E\psi(x,y,z) \tag{2.6}$$

The hamiltonian can now be written using the kinetic energy expressed in terms of the momentum as:

$$H = T + V = -\frac{\hbar^2}{2m^*}\nabla^2 + V, \tag{2.7}$$

with

$$V = 0 \quad \text{for} \quad \begin{matrix} 0 < x < a \\ 0 < y < b \\ 0 < z < c \end{matrix} \quad \text{and} \quad V = \infty \quad \text{for} \begin{matrix} x < 0 \wedge x > a \\ y < 0 \wedge y > b \\ z < 0 \wedge z > c. \end{matrix}$$

Taking into account the conditions inside the box the equation $H\psi = E\psi$ becomes:

$$\nabla^2\psi = -\frac{2m^*}{\hbar^2}E\psi, \tag{2.8}$$

where ψ is commonly referred to as the envelope wavefunction and determines the behavior of the electrons and holes. Elementary quantum mechanics [15] teaches us that the solution can be factored into three functions, each of which is a function of only one variable. Since each function will be independent of any change in the other two variables, each term must be constant $-k_i^2$, with i=x,y,z. The $\sum_{i=x,y,z} -k_i^2$ must be equal to the right-hand side of Eq. (2.8), which is $-2m^*E/\hbar^2$. Therefore, the total energy is the sum of the contributions from each degree of freedom in the x,y and z coordinates. Since the energy associated with any degree of freedom in any single direction is independent of the two other directions, it is possible to write

$$k_i^2 = \frac{2m^*E_i}{\hbar^2} \qquad for \qquad i = x, y, z. \tag{2.9}$$

Thus the Schrödinger equation and the corresponding general solution for single particle in a quantum box results in:

$$\psi_{n_x n_y n_z}(x,y,z) = \sqrt{\frac{8}{abc}}\sin\frac{n_x\pi}{a}x\sin\frac{n_y\pi}{b}y\sin\frac{n_z\pi}{c}z. \tag{2.10}$$

From the solution of the Schrödinger equation we can also deduce that $k_i = \frac{n_i \pi}{a}$ and together with the expressions for the energies using Eq. (2.9), it is possible to define energy levels based on the different components as:

$$E_i = \frac{\hbar^2 n_i^2 \pi^2}{2m^* a^2} \qquad for \qquad i = x, y, z. \tag{2.11}$$

The total energy is

$$E_{n_x n_y n_z} = \sum_{i=x,y,z} E_i = \frac{\hbar^2 \pi^2}{2m^*}\left(\frac{n_x^2}{a^2} + \frac{n_y^2}{b^2} + \frac{n_z^2}{c^2}\right), \tag{2.12}$$

where n_x, n_y and n_z are integers. One quantum number is introduced for each degree of freedom of the system. Therefore, the total energy of the system is dependent on n_x, n_y and n_z. In the case a=b=c, a cubic quantum dot, the denominators of the fractions in Eq. (2.12) are identical. The lowest energy state, referred as ground state, will occur when all the quantum numbers are 1 and this state will be designated as (111). The next lowest energy level will occur when one quantum number is 2 and the others are 1 for example (211), but this state has the same energy as (121) and (112). Therefore, these are degenerate states, in the case of a=b=c. However, if the dimensions of the box are not equal, which is true for most practical cases, the (112), (121) and (112) are not degenerate. An energy level diagram can be obtained and is shown in Fig. 2.2a. The energy level diagrams show the allowed energy states of a QD and is strongly correlated with the density of states as discussed in the previous paragraph. The states are indicated in terms of quantum numbers n_x, n_y and n_z.

Choosing unequal values of a, b and c and then using several integers for the quantum numbers, will enable one to see the nondegeneracy, see Fig. 2.2b. The energy levels can be calculated by using Eq. (2.11) and the actual dimensions of the box and the appropriate constants. Using the dimensions of the dot, see 3.2, the (111) state will be in the order of 130 meV and the intraband level spacing in the order of 15 meV. However, we have to be aware that this is only an estimation for the energy levels.Ultimately, this model will be used to give an approximation for the dimensions of the QD by means of PL lines from a measured spectrum. Although the exact shape of the QDs is unknown, as long as we use this model only to get an estimate of the approximately dimensions of the QD, this model can be applied.

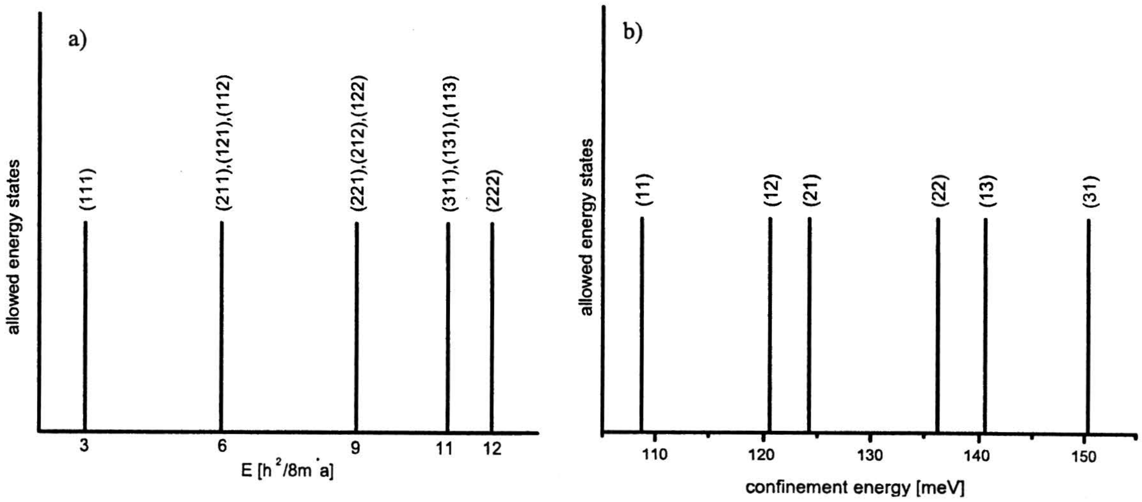

Figure 2.2: *Energy levels for a particle in a three-dimensional box. For a) a degenerate cubic box and b) a rectangular box using representative dimensions (35 x 40 x 8.0 nm*^{3}*) of our QDs.*

In practice, the confinement potential of the quantum dots is not infinite. Therefore, the wavefunctions will be able to penetrate into the barrier, and the energy levels will shift with respect to the situation as described above. It should be mentioned that because of the small z dimension, which leads to large intraband level spacing, we only consider possible configurations of n_x and n_y with n_z fixed to 1. Therefore the different configurations will only be represented by the two quantum numbers n_x and n_y respectively.

2.3.2 Many-body states

In the previous section the behavior of a single electron was examined, but for (opto)electronic applications, these nanostructures need to be filled with one or more carriers. By reducing the dimensions of a structure the interaction between particles will be enhanced. Therefore, the density of states of a many-particle system need not to resemble the one-particle density of states. So it is necessary to take this concept one step further to the many-particle system. Several others have dealt with this concept in different situation as discussed in literature by Dekel *et al* [11], Barenco *et al* [9] and Hawrylak *et al* [10]. The main parameters are now the number and structure of bound single-particle levels, Coulomb interaction among carriers and many-particle interaction which all mainly depends on the number of carriers. The many-body wavefunction $\psi_{n_x n_y n_z}$ for more than one electron is not exactly known. The problem lies in the self-consistency of the solution of the Hamiltonian. The predicted distribution of the carriers itself will depend upon these predicted distribution of the charges itself. In the case of atoms, this is intensively studied and is called the Hartree Fock (HF) [16] approximation. This approximation fails however to incorporate an important characteristic of the electrons and holes. Electrons and holes have non-integer spin and are called fermions. Fermions are characterised by the property that when two fermions of the same spin are interchanged, the wavefunction changes sign. Only linear combinations which are anti-symmetric upon the interchange of two electron indices are relevant. The many-body wavefunction must satisfy the anti-symmetric condition of fermionic wavefunction and this is done by writing it in the form of a determinant. Consequently the many-body wavefunction can be expressed in terms of a product of two determinants, one for spin up and one for spin down. The wavefunction for N electrons will be of the form:

$$\psi = \frac{1}{\sqrt{N\uparrow}} \begin{vmatrix} \phi_{1\uparrow}(x_1,y_1,z_1) & \dots & \phi_{N\uparrow}(x_1,y_1,z_1) \\ \vdots & \ddots & \vdots \\ \phi_{1\uparrow}(x_N,y_N,z_N) & \dots & \phi_{N\uparrow}(x_N,y_N,z_N) \end{vmatrix} \times$$
$$\frac{1}{\sqrt{N\downarrow}} \begin{vmatrix} \phi_{1\uparrow}(x_1,y_1,z_1) & \dots & \phi_{N\downarrow}(x_1,y_1,z_1) \\ \vdots & \ddots & \vdots \\ \phi_{1\downarrow}(x_N,y_N,z_N) & \dots & \phi_{N\downarrow}(x_N,y_N,z_N) \end{vmatrix} . \qquad (2.13)$$

The HF wavefunctions for N holes has identical form. Diagonalisation of the Hamiltonian will lead to the multicarrier energy levels and their corresponding wavefunctions. Because of the self-consistency of this problem, only a first approximation will be used. The single-particle energy levels and wavefunction are used to calculate the exchange and Coulomb interactions. The single-particle energy levels are corrected by the exchange and Coulomb interaction energies. Since this model implies that the electron and hole HF-type wavefunctions are identical the electron and hole distribution throughout the QD are identical too. Therefore the net charge distribution in the QD is zero, in contrast with SAQDs shown in Fig. 2.3. In SAQDs strain-induced polarisation effects take place. Due to expected zero net charge distributions in our strain free QDs no charge polarisation effects will occur.

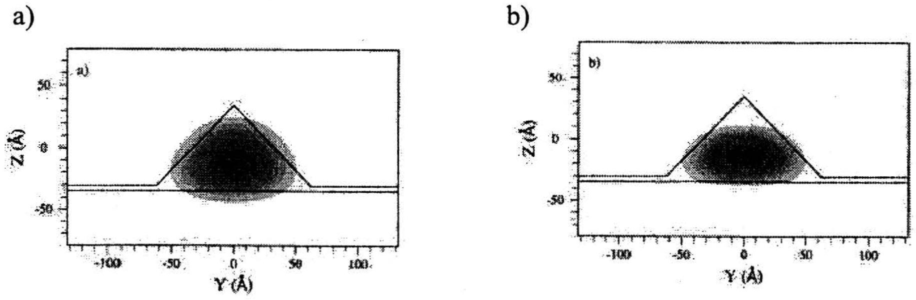

Figure 2.3: *Plot of the wavefunctions for InAs SAQDs through a cross-section for a) electrons and b) holes calculated by Cusack et al. [35].*

In our geometrically non-symmetrical ($a \approx b < c$) box, each of the single carrier state is double spin ($\uparrow\downarrow$) degenerate. The Hamiltonian of an interacting electron-hole system can be written as [11, 10, 9]:

$$H = \sum_{i} H^{e,h}_{free} - \sum_{ijkl} \langle \psi_i^* \psi_j^* | V^c_{eh} | \psi_k \psi_l \rangle + \frac{1}{2} \sum_{ijkl} \langle \psi_i^* \psi_j^* | V^c_{ee/hh} | \psi_k \psi_l \rangle - \frac{1}{2} \sum_{ijkl} \langle \psi_i^* \psi_j^* | V^x_{ee/hh} | \psi_k \psi_l \rangle, \tag{2.14}$$

where ψ_i are Hartree Fock-type electron and hole wavefunction. The first term represents the single particle Hamiltonian, the second the Coulomb attraction between electrons and holes, the third Coulomb term is the mutual repulsion between different electrons or between different holes. The fourth term represent the electron-electron and hole-hole exchange interactions, which only acts upon identical particles with identical spin. The Coulomb potential between the carriers that plays a role in the Hamiltonian then give rise to two-body Coulomb and exchange terms, transforming (2.14) into:

$$H = \sum_{i} H^{e,h}_{free} - \sum_{ij} \langle \psi_i^* \psi_j^* | V^c_{eh} | \psi_i \psi_j \rangle + \frac{1}{2} \sum_{ij} \langle \psi_i \psi_j | V^c_{ee/hh} | \psi_i \psi_j \rangle - \frac{1}{2} \sum_{ij} \langle \psi_i \psi_j | V^x_{ee/hh} | \psi_i \psi_j \rangle, \tag{2.15}$$

The Coulomb and exchange terms are given by the integrals:

$$V^{p/q}_{c,ij} = \langle \psi^p_i \psi^q_j V_{ij} \psi^p_i \psi^q_j \rangle \qquad \text{and} \qquad V^{p/q}_{x,ij} = \langle \psi^p_i \psi^q_j V_{ij} \psi^q_i \psi^p_j \rangle,$$

with p and q the appropriate QD energy levels and $[i, j] \in [electron, hole]$. Notice that the difference in these equations lies in the exchange of particles. These interaction can be calculated by the two-body operator V_{ij}:

$$V_{ij} = \frac{e^2}{4\pi\varepsilon_0\varepsilon_r|\overrightarrow{r_i} - \overrightarrow{r_j}|}, \tag{2.16}$$

where ε_0 and ε_r are the dielectric constants of vacuum and sample material and $\overrightarrow{r_i}$ is the mean radius of the relevant carrier. We will only treat neutral dots in which the carriers are optically excited, although it is also possible to allow analysis of charged dots with this general model. For each electron, a hole is generated as well when using optical excitation for the carriers, maintaining neutrality in the QW. The carriers will subsequently be captured by the QD. However, different capture rates for electrons and holes could lead to a net charge in the QD. Although, once a dot is charged it will attract the opposite charge, which will enhance the capture rate of the opposite charge, keeping charge neutrality in the QD. Therefore it seems valid that we only treat neutral QDs in our experiments.

Exciton complexes

The lowest-kinetic-energy states are obtained by populating the lowest-kinetic-energy single-particle levels of each type of carrier according to the Pauli exclusion principle. Because of the lower effective mass of the light holes, the confinement energy will be higher. Therefore, only the heavy holes are considered when the energy levels are filled with carriers after optical excitation. Since heavy holes have spin $\pm\frac{3}{2}$ and electrons have spin $\pm\frac{1}{2}$, excitons with total spin of $\pm 2, \pm 1$ will be formed. However, only excitons with total spin of ± 1 are optically active while excitons with total spin of ± 2 are dark excitons. One exciton corresponds to an electron and a hole occupying their lowest-kinetic-energy state, as shown in Fig. 2.5. According to equation (2.17) the total exciton ground state energy is given by the electron and hole single-particle energy corrected by their mutual Coulomb attraction, which is the exciton binding energy,

$$E_X^0 = E_{11}^e + E_{11}^h - \underbrace{\langle 11; 11|V_{eh}|11; 11\rangle}_{V_{c,eh}^{11/11}} . \tag{2.17}$$

Where $\langle 11|$ represents the HF-type wavefunction for a carrier in energy level (11). Since there is only one electron and one hole, the exchange interaction does not have any influence yet. The exciton state is double degenerate due to spin. For the two-exciton complex there is only one lowest-kinetic-energy configuration possible, see Fig. 2.5. The biexciton ground state energy is twice the single exciton energy plus an extra many-body term, which leads to the following result:

$$E_{2X}^0 = 2E_X^0 + \underbrace{\langle 11; 11|V_{ee}|11; 11\rangle + \langle 11; 11|V_{hh}|11; 11\rangle - 2\langle 11; 11|V_{eh}|11; 11\rangle}_{V_c^{11/11}} . \tag{2.18}$$

with $V_c^{11/11}$ known as the biexciton binding energy, see Fig. 2.4.

The first term is the single exciton energy, the next two are the electron-electron and hole-hole repulsion respectively and the last is the Coulomb electron-hole attraction. These terms make up the biexciton binding energy as shown in Fig. 2.4. Again the exchange interaction is still left out, because there is only one possible configuration due to the Pauli exclusion principle. Since there is only one singlet for electrons and holes, the ground state is not degenerate. Therefore there are no dark biexciton states due to spin.

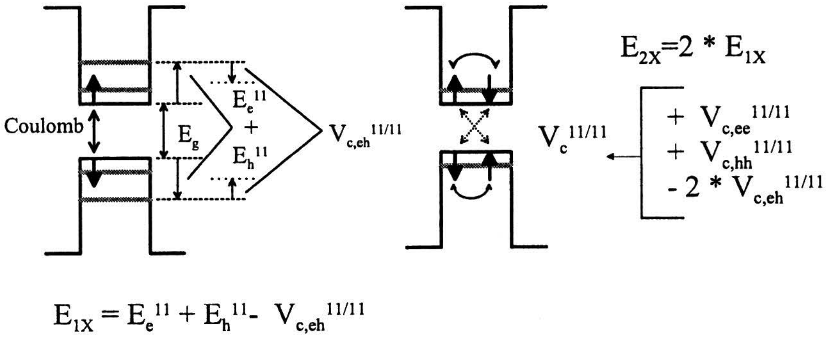

Figure 2.4: *Energy contributions to a) the single exciton and b) the biexciton.*

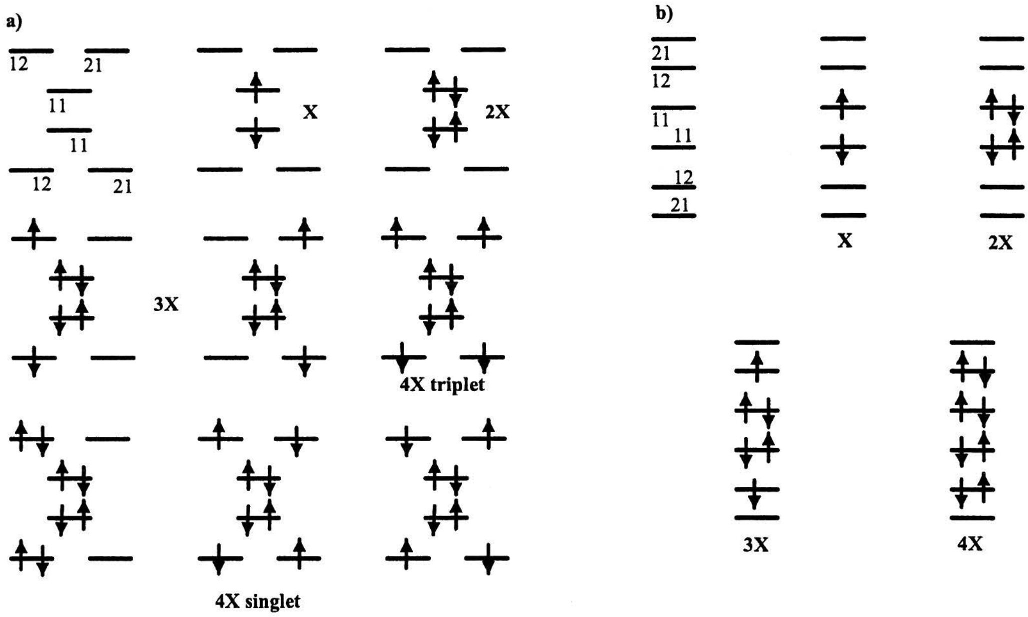

Figure 2.5: *Overview of the lowest kinetic energy configurations of exciton complexes in a) degenerate system [10] and b) non-degenerate system.*

The three exciton case is somewhat more difficult to describe, this is because the possibility of degeneracy of the (12) and (21) energy levels, see Fig. 2.5. In the case of an asymmetric dot the energy levels will be degenerate and the lowest energy levels of the two will be populated. We shall assume that the (12) state is the lowest energy level of the two and therefore will be populated first in the case of asymmetry. In the case of a symmetric dot, the energy levels are degenerate and the possibility to populate either of the two energy levels is the same. Electron-hole interaction allows the electron-hole pair to scatter from the (21)(21) state to the (12)(12) state and mixes quantum mechanically the two configuration, see Fig. 2.6. As the electron-hole pair can be in either of the two degenerate states, the ground state energy for a three-exciton complex results in:

$$E_{3X}^{\pm} = E_{2X}^{0} + E_{12}^{e} + E_{12}^{h} - V_{c,eh}^{12/12} - V_{x}^{11/12} + 2V_{c}^{11/12} \pm \langle 12;12|V_{ee/hh}^{s}|21;21\rangle. \tag{2.19}$$

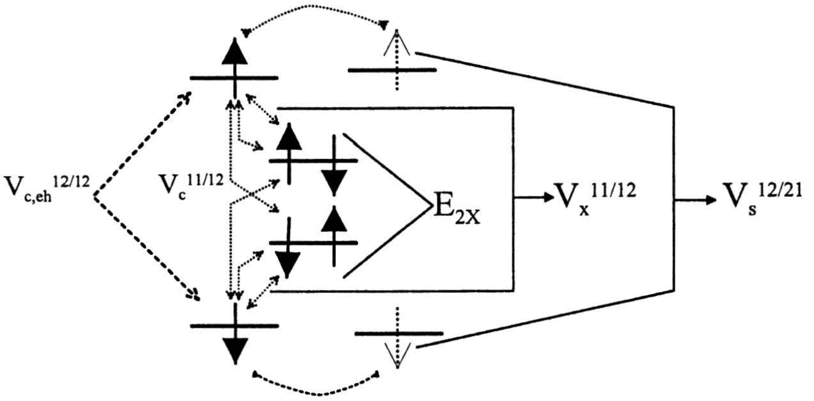

Figure 2.6: *Energy contributions to three exciton complex in a degenerate system.*

Where $V_x^{11/12}$ represents exchange interactions between identical carriers with identical spin of (11) and (12), and V_{ii}^{s} represents scattering, which is only present in degenerate configurations. It turns out that only one of the two degenerate configurations is optically active due to scattering. The lowest energy level, E_{3X}^{-}, will be populated and corresponds to the optically active configuration. Note that in the case of an asymmetric dot the scattering potential disappears and consequently there is only one possible configuration, which is optically active. It should be mentioned that additional Coulomb interaction occur due to direct attraction/repulsion between electrons and holes in different energy states, compared to the biexciton complex. A schematic summary of different mechanisms leading to shifts in energy levels is shown in Fig. 2.7.

In the three exciton configuration, either the exciton in (11) or (12) can recombine resulting in three different recombinations: 3X → 2X, 3X → $2X^{*s}$ or → $2X^{*t}$. The indices 's' and 't' indicate singlet (antiparallel spin alignment of the carriers) and triplet (parallel spin alignment) configuration respectively, see Fig. 2.8. When an exciton of the (11)

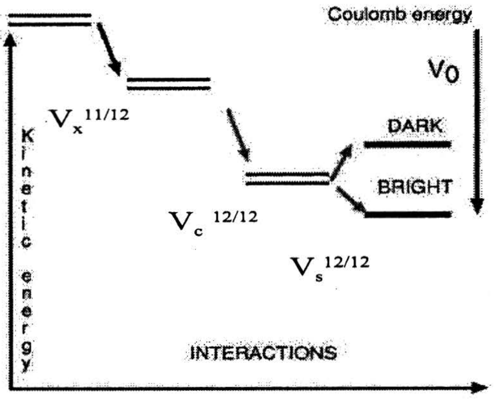

Figure 2.7: *Overview of interaction contributions to energy levels in a degenerate system of the three exciton complex [10].*

energy level recombines this is defined as s-shell recombination. PL lines originating from recombinations of an exciton either from the (12) or (21) are called p-shell recombinations, see Fig. 2.9. Recombinations of p-shell excitons have a higher photon energy, because of the higher confinement energy of the carriers which recombine.

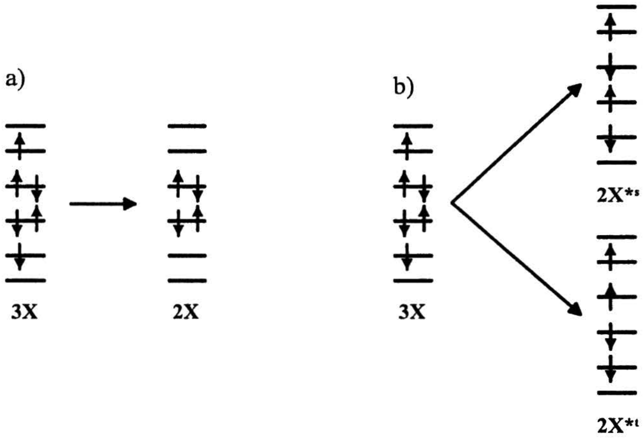

Figure 2.8: *Three exciton recombinations, a) for s-shell recombination and b) p-shell recombination.*

The four exciton complex can also be more difficult to describe, depending on whether the dot is asymmetric or not. For a complete overview in the case of a symmetric dot,

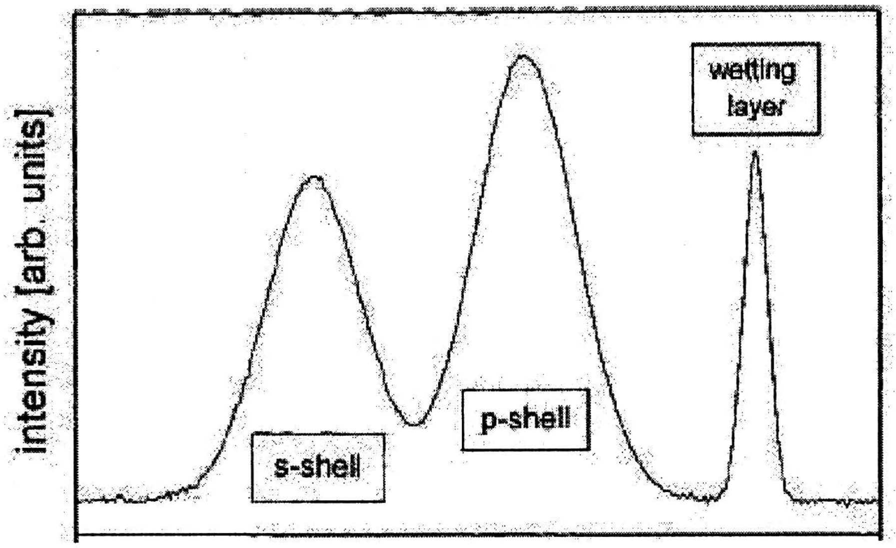

Figure 2.9: *Recorded PL spectrum with only two electronic shells occupied, leading to s- and p-shell recombinations [17].*

see Hawrylak *et al.* [10]. For practical reasons, we assume that we deal with asymmetric dots and consequently non-degenerate states. Therefore, the fourth electron-hole pair will resemble the case of the biexciton case. There is only one possible configuration of the ground state for the fourth electron and hole to fill the energy levels due to the Pauli exclusion principle. The state filling for five or more excitons is analogous to the state filling of the first two energy levels as discussed before.

It is also possible for exciton complexes to occupy an excited state. These excited states are characterised by promoting one or more excitons to a higher energy level. For an excited single-exciton with the electron-hole pair in the (12) state the energy can be written as:

$$E_X^{'} = E_{12}^e + E_{12}^h - V_{c,eh}^{12/12}. \tag{2.20}$$

For excited two exciton complexes, different configurations are possible. This depends upon whether the spin of the electrons/holes are parallel or anti-parallel. If the spins are aligned in the same direction, an exchange interaction will be present. However in the case of anti-parallel spin alignment, this exchange interaction will be missing. The energy of an excited two exciton complex depends on the configuration of the carriers, see Fig. 2.10.

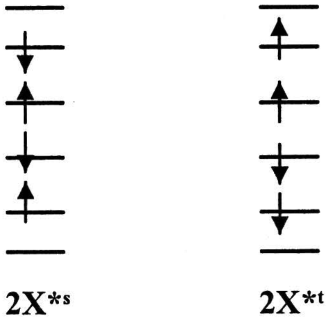

Figure 2.10: *The two first excited biexciton configurations, a) singlet and b) triplet.*

For the singlet state the energy can be written as:

$$E'_{2X} = E^e_{11} + E^h_{11} + E^e_{12} + E^h_{12} - V^{11/11}_{c,eh} - V^{12/12}_{c,eh} + V^{11/12}_{c}. \tag{2.21}$$

Because of the opposite spin alignment of the carriers in (11) and (12) the exchange term will not come into play for this configuration. The energy for the triplet configurations is defined as:

$$E'_{2X} = E^e_{11} + E^h_{11} + E^e_{12} + E^h_{12} - V^{11/11}_{c,eh} - V^{12/12}_{c,eh} + V^{11/12}_{c} - V^{11/12}_{x}. \tag{2.22}$$

The energy of a triplet state has a lower total energy, as can be seen from equations (2.21) and (2.22). It depends on the relaxation, see section 2.5, which configuration the electron and hole will finally occupy. Hund's rules determine which few-electron configuration in atoms can give contribution to photoluminescence spectrum. Hund's rules say that when all quantum numbers are equal, the state with the highest total spin will have the lowest energy and therefore will most probably be occupied. Furthermore, Hund's rules say that electrons should be distributed as much as possible over degenerate energy levels and that electrons should be placed with identical spin in degenerate energy levels. However, we are populating energy levels with two types of particles, electrons and holes. The hidden symmetries in the PL spectrum due to the many-particle states results an analogue of Hund's rules for real atoms.

2.4 Optical Properties

To discuss the optical properties resulting from discrete energy levels, the probability of dipole-allowed optical transitions has to be evaluated

$$\alpha(\omega) \sim |\langle \Psi_f | \widehat{P} | \Psi_i \rangle|^2 \tag{2.23}$$

with $\widehat{P}$ the dipole operator. Ψ_i and Ψ_f are the initial and final state of the optical transition. Considering only the interband part, the overlap integral reads as

$$\langle f | \widehat{P} | i \rangle = \underbrace{\langle u_{\nu f} | \widehat{P} | u_{\nu i} \rangle}_{p_{cv}} \langle \psi_f | \psi_i \rangle, \tag{2.24}$$

where

$$\begin{aligned} |i\rangle : \quad & \Psi_i = u_{\nu i} \cdot \psi_i, \\ |f\rangle : \quad & \Psi_f = u_{\nu f} \cdot \psi_f \end{aligned}$$

The integral can be separated into the integration of the fast oscillating Bloch part u_ν and the integration of the envelope partψ. The integration of the Bloch part results in the size independent dipole matrix element p_{cv} of the bulk. Despite the different behavior of the electrons and holes in quantum dots, there is an analogy with the optical transitions of excitons in bulk material. The transition probability for the exciton in bulk is proportional to the probability of finding the electron and hole in the same unit cell of the crystal. The oscillator strength f_X is proportional to the volume in k-space necessary to form the exciton [19], i.e. the inverse of the exciton volume πa_X^3,

$$f_X \sim \frac{|p_{cv}|^2}{\pi a_X^3}. \tag{2.25}$$

In quantum dots the transition probability is proportional to the spatial restriction of carrier motion in the quantum dot volume due to the externally imposed quantum confinement, as shown in equation (2.23). The quantum dot specific selection rules of interband transitions between confined electron and hole states are obtained by integrating the envelope functions ψ over the quantum dot volume. Due to the orthonormality of the envelope functions ψ_i and ψ_f, the integration yields delta-functions. The well-known selection rules are obtained, all transitions that conserve n and l (angular momentum) are allowed between non-interacting electron and hole states. The oscillator strength of these transitions is proportional to $(2l+1)$ due to the summation over all states with $-l \leq m \leq l$ contributing to the absorption. Optical transitions at the energies $\hbar\omega = E^e_{nl} + E^h_{nl}$ above the band gap will occur and for the absorption coefficient hold

$$\alpha(\omega) \sim |p_{cv}| \frac{1}{\frac{4\pi}{3}R^3} \sum_{n,l} (2l+1)\delta(\hbar\omega - E^e_{nl} - E^h_{nl}). \tag{2.26}$$

However, degeneracy in angular momentum does not occur in our rectangular QDs, thus we can neglect the degeneracy in angular momentum. Comparing the bulk exciton oscillator strength with that of electron-hole pairs in quantum dots, (2.25) and (2.26), results in

$$\frac{f_{QD}}{f_X} \sim \frac{a_X^3}{R^3} \tag{2.27}$$

and an enhancement of the oscillator strength becomes evident when the size of the quantum dots decreases below the Bohr radius. It should be noted that this picture is simplified for an ideal case. It has been shown [20, 17] that dots (even of the same sample) exhibit strong variations of their symmetry. These variations are reflected by the optical properties of quantum dots. In these samples, a splitting of the absorption spectrum into multiple lines has been observed [18, 17], when higher electronic states in the dot appear. The splitting has been shown [21] to be an example of nontrivial mixing of resonant electron-hole pairs, which couples only with coherent photons, in the interacting quantum dot complex. More realistic quantum dots could have a negative influence on the oscillator strength, it will however not cancel out the effect of reduced dimensionality.

2.5 Carrier Relaxation

Particularly in the case of the photoluminescence emission spectrum, the possibility of observing higher-energy peaks, depends on two competing processes.(i) Carrier relaxation, which can be subdivided into spin related relaxation and carrier related relaxation mechanisms. (ii) Radiative recombination, which can be subdivided into radiative and non-radiative recombination. As a result of the optical properties of QDs, the usual $\Delta k = 0$, selection rule of optical transitions has to be refined. Electron and hole states can decay radiatively only if they have exactly the same quantum number $\Delta_{n_x,n_y,n_z} = 0$. The most significant mechanism of carrier relaxation in semiconductor structures are the interactions with longitudinal (LO) phonons. Alternative nonlinear relaxation mechanisms, like

Coulomb scattering (electron-electron, hole-hole or electron-hole) [22] or Auger recombination are expected to become important with increasing carrier density. In typical 3D and 2D (Quantum Well) systems, electrons meet holes both in real and k space, see fig 2.11. The elastic collisions between carriers very quickly randomise k directions, resulting in a thermal equilibrium. Energy is lost first through LO phonon emission (timescales of $10^{-12} - 10^{-13}$ s) and next through acoustic phonons (timescales of 10^{-9} s) due to the 2D continuum of final states.

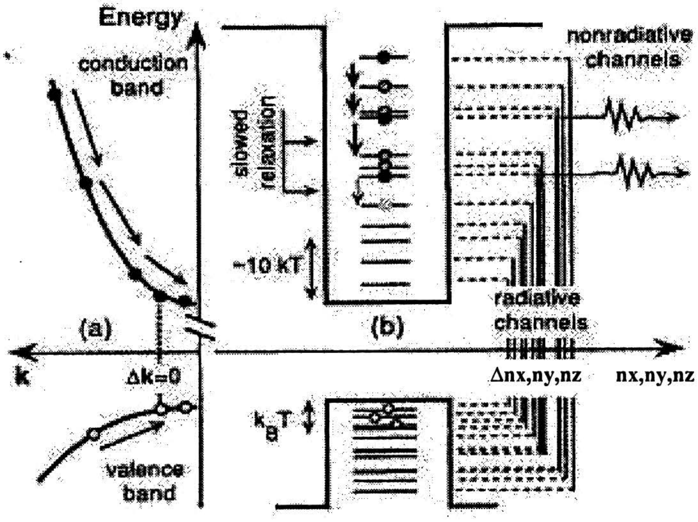

Figure 2.11: *(a) Energy relaxation in a continuum. Radiative recombination is possible even though k=k' is needed because both band edges are populated. (b) Energy relaxation through fully=quantised box levels can be very slow, [24].*

The relaxation of an exciton, which is confined in a quantum dot , through emission of an optical phonon LO is rather inefficient. Two problems have been proven to be essential in the course of this discussion. The first one concerns the energy separation between the confined levels of the quantum dots. When decreasing the sizes of quantum dots, the spacing between the confined energy levels increases and the energy distance can become larger than the phonon energies. The phonon energy is almost constant ($E_{LO} = 36.2$ meV for GaAs) and therefore the first-order process (with the emission of a single phonon) requires a precise fitting of the distance between two discrete energy levels and the phonon energy

E_{LO}. A dramatic modification of the electron and hole relaxation process can occur because of the lack of lower/higher energy states of electrons and holes matched in energy for the phonon absorption and emission. In high quality samples and at low excitation densities the relaxation through the ladder of excited states can only proceed via inefficient multiphonon processes [23] or acoustical phonons. The second consists in the number of states acting as free final states for scattering processes, which is drastically diminished in quantum confined structures. The finite degeneracy of each QD state leads to state filling effects already when few carriers populate the lowest dot states. Thus carrier relaxation from excited states to energetically lower dot states (inter-dot relaxation) should be hindered already at low excitation densities (Pauli blocking [12]). Both these considerations have led to speculations about the suppression of the carrier relaxation rate within the ladder of the confined energy levels and the existence of the so called "phonon-bottleneck". It was concluded by Benisty *et al.* [24] that the suppressed excited carrier relaxation presents an intrinsic mechanism for the poor luminescence of quantum dot structures.

However, a number of experiments have been published which do not indicate the appearance of a phonon-bottleneck or reduced relaxation rates in QDs. Generally, the theoretical results show that interaction with acoustic phonons can not remove the problem of the phonon-bottleneck. Apparently, alternative mechanisms come into play such as Auger-like processes where the energy relaxation is mediated by an electron-hole plasma [25], via energy transfer from the electron to the hole and fast relaxation within the hole subsystem [26]. Sosnowkski *et al.* [22] reported that electron-hole scattering already at low excitation densities can reduce relaxation times drastically. Lattice imperfections can also contribute to the relaxation of carriers. In SAQDs a strain-induced polarised exciton is present, which is expected to enhance the Fröhlich interaction according to Minnaert *et al.* [27] resulting in a fast carrier relaxation. Brunner *et al.* reported to have observed slowed energy relaxation for GaAs/AlGaAs QDs[28], which are strain free. If one believes that the carrier relaxation in our strain free QDs, circumventing strain induced polarisation effects, can be considerably slowed down, observation of a phonon bottleneck could be possible.

Chapter 3

Experimental Setup

3.1 Introduction

From an experimental point of view, single QD spectroscopy would be the technique of choice for investigations in optical properties. For a fundamental understanding of the optical properties of a QD, one has to get rid of all background signals, which might disguise the optical spectra and hence complicate comparison to theory. Experimental methods with extremely high spatial resolution are required to isolate the dots for advanced spectroscopic analysis. Therefore a high resolution PL setup is used which allows us to perform confocal PL microscopy even in cryogenic environments. The main advantage of such a system is the high collection efficiency and the ability to get images.

3.2 Sample

As described in the introduction 1.2, it is possible to grow QDs on predefined positions and with reduced size fluctuations. The sample under investigation has these characteristics and is grown by R. Nötzel *et al* [4]. A method for improving size uniformity, while maintaining a high density is used, that combines elements of both self-organisation and patterning. For a detailed description of the procedure see [4]. Here a brief outline will be given. Starting with a two dimensional GaAs/AlGaAs quantum well grown by MBE on patterned GaAs (311)A substrates, the evolution of a fast-growing sidewall for mesa stripes along the $[01\bar{1}]$ directions is observed [29]. The sample is prepared by optical lithography and wet chemical etching in such a way that stripes orientated along the $[01\bar{1}]$ direction are formed. These stripes have a periodicity of 300 μm, see Fig. (3.1).

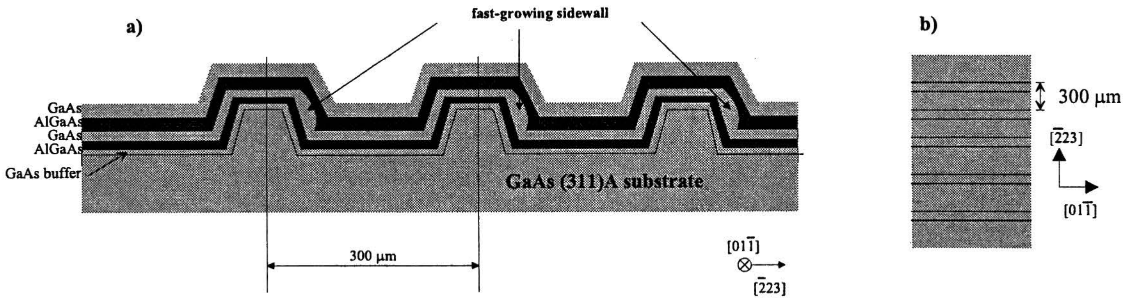

Figure 3.1: *Schematic illustration of the quantum dot sample, a) cross-section and b) topview.*

The complete growth sequence consisted of a GaAs/$Al_{0.7}Ga_{0.3}As$ double heterostructure on a GaAs buffer layer. A GaAs quantum well, with AlGaAs barriers, is formed over the entire substrate. However, the evolution of a fast-growing sidewall is only present on one side of the etched stripes pattern. A quantum wire structure is enclosed with a height of approximately 6 nm and a width of approximately 40 nm. If atomic hydrogen is added during MBE growth on GaAs (311)A substrates, natural one-dimensional surface corrugations on the nanometer scale form in the $[\bar{2}33]$ direction, which is perpendicular to the stripe direction mentioned above. These corrugations have a lateral periodicity of approximately 40 nm and are straight over several micrometers. With the supply of atomic hydrogen, the natural one-dimensional surface corrugation along $[\bar{2}33]$ direction is also established on the convex curved part of the sidewall. Due to this effect, the quantum wire is subdivided into pieces by the step bunching. Therefore the presence of dot-like nanostructures are observed in the corrugated GaAs layer which is embedded between the two lower and upper AlGaAs barrier layers, see Fig. (3.2). This mechanism described above can be used as a template for the formation of nanostructures.The photoluminescence spectra is dominated by one single sharp peak (FWHM = $\pm$ 70 μeV) without background emission over a large energy range, see Fig. 3.3.

If only a small fraction of the dots were of equal size, emission of either a number of sharp peaks or an inhomogeneous broadening would occur; this was not observed by Nötzel *et al* [4]. Thus, the atomic hydrogen induced periodic step bunching removes the random interface fluctuations along the wires while the random interface fluctuations along

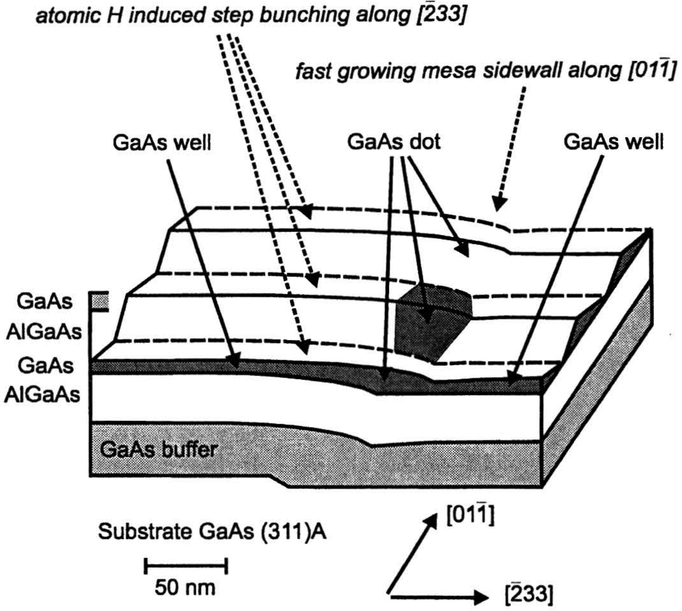

Figure 3.2: *Schematic illustration of the quantum dot array.*

the step bunches in the corrugated quantum well are removed by the well defined wire width in patterned growth. The result is a uniform array of QDs. Because on high index surfaces less step edges occur compared to low index surfaces this effects is even enhanced. Moreover, the spectra of the QD array remain unchanged when the optical probing is increased to several micrometers, corresponding to the probing of several hundreds of dots. Note that the QDs formed by this growth mechanism are strain free. The density of the dots in the one-dimensional array is 1.5 10^5 cm^{-1}. The background contaminations of the QD sample is in the order of 10^{13} cm^{-3}. The QDs formed by this method are more or less rectangular boxes with the dimensions of approximately 40 x 40 x 6 nm, measured by Atomic Force Microscopy (AFM) and cross-sectional Transmission Electron Microscopy (X-TEM). Therefore the excited states are non-degenerate in both perpendicular in-plane directions. The collected photoluminescence is characterised by a narrow peak in the spectra, with small asymmetric broadening in the sharp PL peak, see Fig. 3.3. This is an indication for small size fluctuations between the homogeneous QDs.

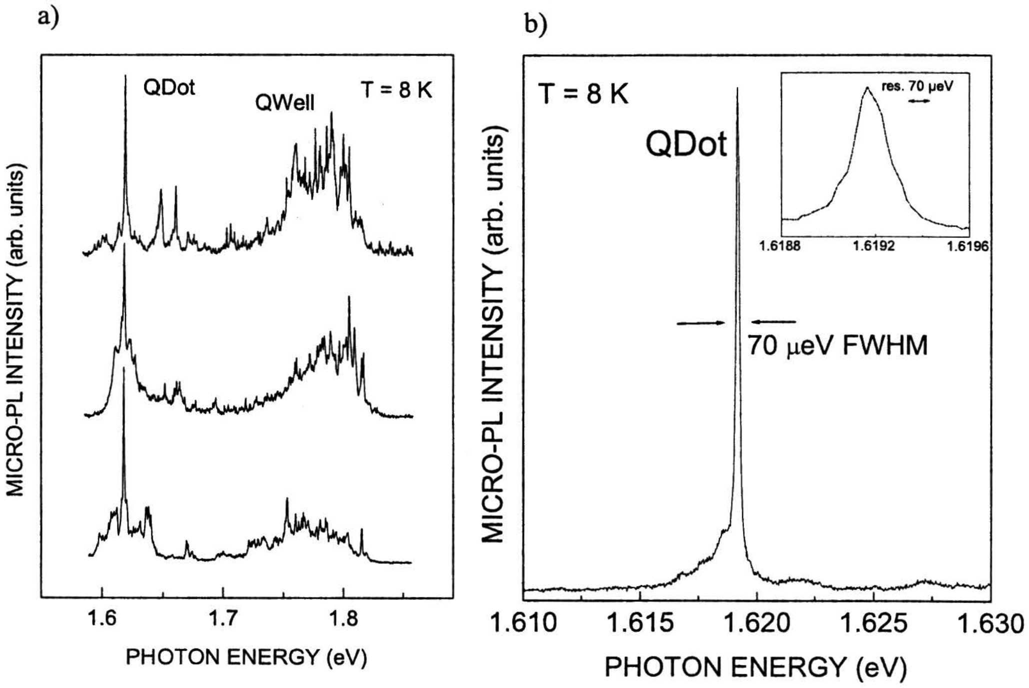

Figure 3.3: *Optical properties of the QD-array. a) Micro-PL spectra taken at 8 K at different positions at the Qwire. The diameter of the excitation spot is reduced by confocal imaging system to 2 μm with an excitation power of 0.1 mW. b) High resolution μ-PL of the QD-array [4].*

As discussed already in 2.2.2 it is difficult to say in which confinement regime the excitons are. Considering the Bohr exciton radius and the lateral dimensions, the excitons are confined weakly. However, there is a relatively large band gap energy difference however between GaAs and $Al_{0.7}Ga_{0.3}As$ i.e. the band gap energy for GaAs is 1.52 eV and for $Al_{0.7}Ga_{0.3}As$ 2.49 eV at 5K.

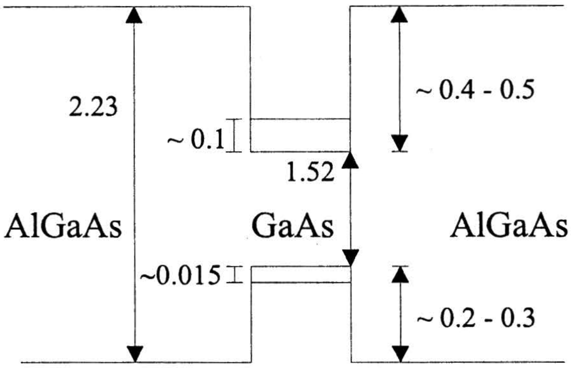

Figure 3.4: *Schematic overview of band gap energy for the* $Al_{0.7}Ga_{0.3}As/GaAs$ *heterostructure. Numbers shown are energy differences in eV.*

Therefore the resulted AlGaAs/GaAs heterostructure which is formed after the growth sequence will have a large confinement potential, see Fig. 3.4, due to the band gap energy difference between GaAs and $Al_{0.7}Ga_{0.3}As$. The groundstate energy is typically in the order of 100 and 15 meV for electrons and holes respectively. The ratio of groundstate energy and the confinement potential is high which indicates strong confinement for the carriers in the QD. Consequently, the excitons are weakly confined by the QD dimensions, but the carriers are strongly confined by the confinement potential. The confined carriers will feel primarily the dielectric constant of GaAs, which is important for the Coulomb interaction, see equation (2.16). Therefore it is necessary to quantise both the electron and hole motion. It should be mentioned that the confinement potential is not uniform in all three directions, due to the complex growth mechanism. Therefore this is only used as a model to be able to make an approximation for the relevant properties, such as Coulomb interactions.

3.3 Monochromator

In order to have an high spectral resolution for the collected photoluminescence a Jobin-Yvon triple spectrometer was used to disperse the light. The T64000 triple spectrometer delivers a high performance in resolution, stray light rejection and imaging capabilities. The instrument is based on a triple 0.64 meter focal length mononchromator, which result in a total focal length of 1.92 meter in additive configuration. It should be mentioned that the major part of the measurements are carried out in subtractive mode. Depending on the requirements, different configurations are possible for the monochromator. The first two monochromators are referred to as foremonochromator and the third is referred to as spectrograph. Because the gratings are kinematically mounted and driven with a sine bar, the instrument will operate over a large spectral range. The step size of the sine bar is 0.01 Å based on a 1200 gr/mm grating. The monochromator can be used as a triple spectrometer with the double foremonochromator usable as a subtractive filter or as a double additive dispersive system for ultimate resolution. The monochromator is equipped with two independent sine bars. One is scanning the gratings of the foremonochromator and the other one is scanning the spectrograph. The gratings of the foremonochromator are mounted on a single sine bar, which maintains the correct alignment of the two gratings. Our system is delivered with two different sets of gratings; a set of gratings with 1200 gr/mm and with 600 gr/mm. For specifications for the different gratings, see table 3.1.

Table 3.1: *Specifications for the monochromator system.*

		Subtractive		Additive	
Grating (gr/mm)	Mechanical Range	Monochannel Resolution [Å]	Multichannel Coverage [Å]	Monochannel Resolution [Å]	Multichannel Coverage [Å]
600	0-3000 nm	0.54	520	0.18	175
1200	0-1500 nm	0.27	260	0.09	87

In the double subtractive configuration, the double subtractive foremonochromator is used as an tunable filter in the spectral range defined by the scanning mechanism and the gratings. Light which enters the first monochromator through the entrance slit is dispersed by the first grating. The exit slit of the first part of the foremonochromator (the entrance slit of the second part of the foremonochromator) selects a bandpass between λ_1 and λ_2.

In the subtractive configuration the grating in the second monochromator recombines all the dispersed radiations on the exit slit of the second monochromator (the entrance of the spectrometer). This radiation contains again a range of wavelengths, but now limited by the spectral range between λ_1 and λ_2, see Fig. 3.5. The grating of the third stage of the monochromator will again disperse the radiation. The spectrum is acquired with a multichannel detector in the plane of the exit image or with a monochannel detector through an exit slit. The effective focal length in this configuration is only 0.64 m. For optimal use of this configuration, two criteria must be considered. First the width of the slit $S_{i2/3}$ must be equal to the width of the entrance slit in order to couple foremonochromator and spectrograph correctly. And second the width of slit $S_{i1/2}$ must be equal to the length of the multichannel detector for its full coverage.

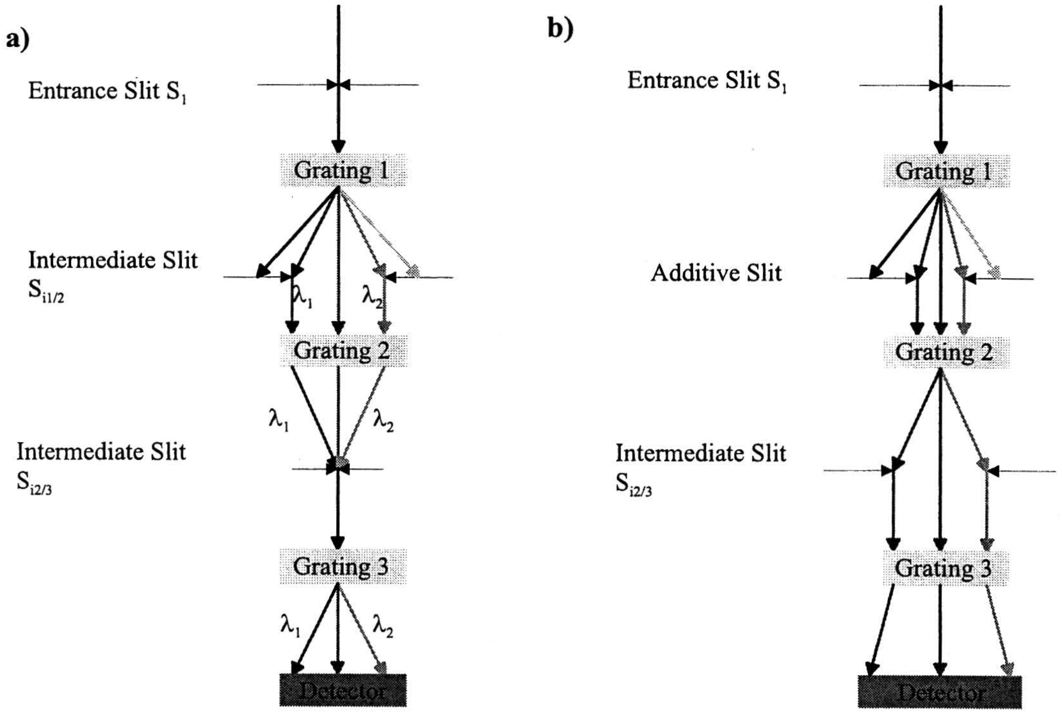

Figure 3.5: *Overview of monochromator in a) subtractive and b) additive configuration.*

In the triple additive configuration the monochromator permits to obtain a high resolution, because the light is dispersed in each stage of the monochromator, see Fig. 3.5. The triple additive dispersion is equivalent to a spectrograph of 1.92 m focal length, which results in a three times better resolution than in subtractive mode. When a multichannel detector, for example a charge couple device (CCD) camera, is used in the triple additive configuration, only the entrance slit S_1 is narrow, defining the resolution. All other slits should be widely opened for the largest coverage on the CCD camera. The monochromator is driven by the a custom software program, Labspec which is also operating the monochannel detector.

To be able to fulfill the specifications of the monochromator, the system must be calibrated and verified against the specifications. The calibration and determination of the resolution has been done with a Xenon lamp, which is placed exactly in front of the entrance slit S_1. In this way the Xe-lamp is positioned as close as possible at the optical axes and acts as a point source. Determination of the resolution for each individual stage is done by narrowing the entrance and exit slit of each individual stage with all other slits widely opened. For example to determine the resolution of the second stage, the intermediate slits $S_{i1/2}$ and $S_{i2/3}$, which act as entrance and exit slit respectively, are narrowed to approximately 30 μm. Subsequently a small wavelength scan is made and the Xe-peak is recorded by a monochannel detector. After calibration of each individual stage, the wavelength of the double foremonochromator is calibrated and the resolution is determined. Because the two stages of the double foremonochromator are mounted on the same stepping mechanism the wavelength can only be calibrated for the double foremonochromator and not for the individual stages itself. The spectrograph is moving independently and therefore also the wavelength can be calibrated independently. By calibration of the foremonochromator and the spectrograph, the total monochromator system is calibrated in wavelength on the Xe-peak. Hereafter it is possible to determine the resolution of the foremonochromator and the total monochromator system both in subtractive and additive mode. The results of the resolution determination are shown in table 3.2. These values are valid for the monochromator system with 1200 gr/mm gratings. The entrance and exit slits were narrowed to 30 - 40 μm. The given specifications for the monochromator are 0.27 Å and 0.09 Å for triple subtractive and triple additive mode respectively, see table 3.1. Unfortunately, the specifications are not fully achieved, which can be caused by the following. The positioning of the Xe-lamp in front of the entrance slit is quite critical. It is not possible to place the Xe-lamp exactly in the plane of the entrance slit but just in front of it and therefore the light rays emitted by the Xe-lamp can slightly deviate from the optical axis. Secondly, the internal alignment is not perfect either, because we often changed the set of gratings. A light beam which enters the entrance slit completely in the center and which is reflected

Table 3.2: *Measured resolution for the monochromator system with 1200 gr/mm gratings.*

Stage	subtractive [Å]	additive [Å]
Mono 1	0.36	idem
Mono 2	0.20	idem
Double	0.40	0.19
Mono 3	0.37	idem
Triple	0.38	0.18

by first grating also in the center is not going through all centers of the intermediate slits. This means that one or more elements of the internal alignment of the monochromator are not perfect. These two imperfections can cause the beam to deviate from the optical axis. Hence the beam can be stopped by one of the slits if they are being narrowed. To prevent that the light beam is stopped by one of the slits, the slits must be opened further. This implies that the resolution is becoming worse, because the resolution is determined by the slit opening. Despite these imperfections, the obtained resolution is sufficiently high for the intended measurements and we did not try to further optimise the system.

3.4 Photoluminescence Setup

Photoluminescence measurements are the basic tool that allow for the investigation of discrete energy levels of QDs. See for a global overview of the PL setup Fig. 3.6. The sample, which is placed in a Helium flow-cryostat (b),see 3.4 and cooled down to 5 K, is excited by a laser system (a). Two different laser systems are used; a pulsed and a continuous wave (cw) laser system. A Helium-Neon (He-Ne) laser is used for the cw laser, emitting at 633 nm. For the pulsed laser systems two different laser were available; a Yttrium Aluminium Garnet (YAG) pumped dye laser, which is tunable between 550 - 650 nm and a Ti:sapphire laser, which is tunable between 700 and 1000 nm. The laser beam is reflected by an semi-transparent mirror onto the sample and is focussed by a Newport F-LA15 aspheric lens (l) with a numerical aperture of 0.5. The lens has a focus distance of 2 mm, an aperture of 2 mm and a minimum spot size of 1.8 μm. The excitation spot is imaged by a CCD video camera module on a monitor(h). The focus of the excitation beam can be checked on the monitor. The emitted photoluminescence (PL) is also collected by this lens and is guided through the semi-transparent mirror into the monochromator.

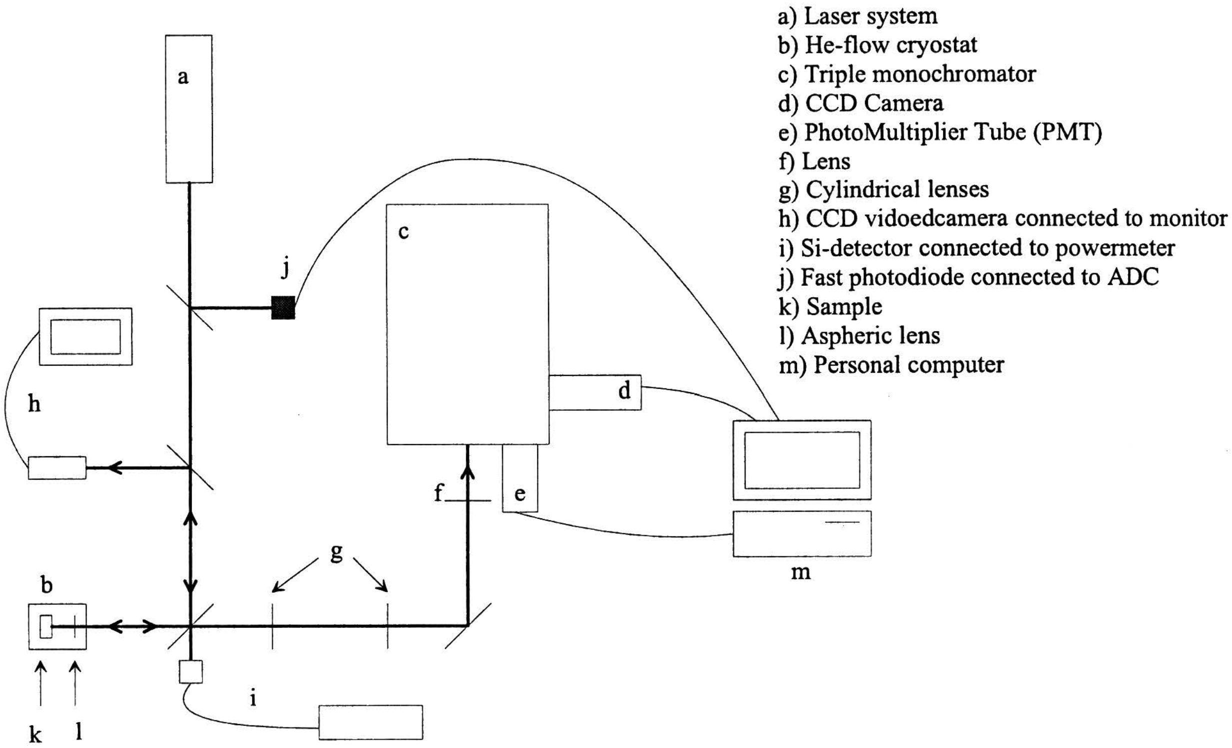

Figure 3.6: *Schematic overview of the photoluminescence setup.*

The previously discussed monochromator is a key element in the experimental setup for high resolution photoluminescence. The most important issue is to find the optical axis of the monochromator, in order to have the correct coupling of the light into the monochromator. Several adjustable mirrors and lenses are placed in front of the monochromator to be able to steer the light beam to coincide with the optical axis. The aperture of the lens in front of the monochromator has to meet the requirement of f/7.5 to illuminate the entire gratings for optimal resolution. The optical axis is found when a light beam enters the entrance slit in the center and also illuminates the center of the first grating. By narrowing the slits, adjusting the mirrors and lenses and monitoring the illumination of the first grating the optical axis is found. The PL is subsequently dispersed by the monochromator (c) and detected by a 2-dimensional CCD camera (d) or a Photo Multiplier Tube (PMT) (e). A movable mirror just in front of the exit slit of the monochromator, driven by the monochromator software makes it possible to switch between the CCD camera and the PMT. The deep depletion silicon 2-dimensional, 1340 x 100, array CCD camera with a pixel size of 20 x 20 μm, is cooled with liquid nitrogen. The CCD camera, which has the best quantum efficiency from 700 to 900 nm, allows us to image the light emitted or reflected by the sample. The advantage of the CCD camera over the PMT is the ability to make an instant wavelength scan over a large range. Imaging the laser spot on the sample with the CCD camera, it appeared that the spectral and spatial focus distances were not the same. This astigmatism of the monochromator was corrected by two cylindrical lenses (g) in front of the monochromator.

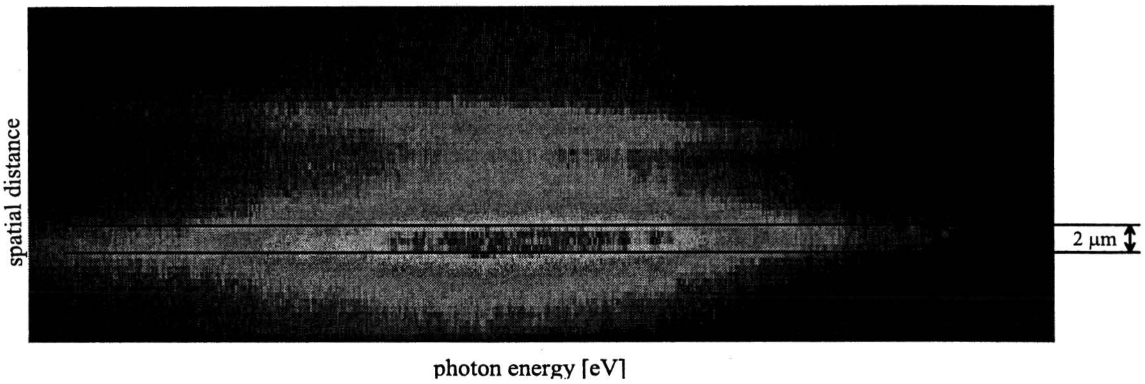

Figure 3.7: *Image of the GaAs QW PL. The photon energy is plotted along the horizontal axis and the spatial distance in one direction of the sample along the vertical axis.*

To check the correction for astigmatism the PL of the GaAs Quantum Well (QW) is imaged by the CCD camera. The distance between the two cylindrical lenses is varied such that the image of the GaAs QW PL is at his narrowest. This also determines the spot size on the sample, see Fig. 3.7. The spot size is calculated, from Fig. 3.7 together with the magnification of the lens systems, to be approximately 2 μm. The next step is finding the QDs by scanning the laser spot over the sample with the help of the micrometer screws. Having found the position of the QD array, the PL emitted by the QDs can be detected. The size of the laser spot corresponds with the excitation of approximately 25 QDs. The excitation power is measured with Si-photodetector connected to a digital Newport 835 digital power meter (j). A polarising filter between the cryostat and the monochromator can be added to the setup for polarisation dependent measurements.

Cryostat

A He-flow cryostat is used with a home built insert, see Fig. 3.8.

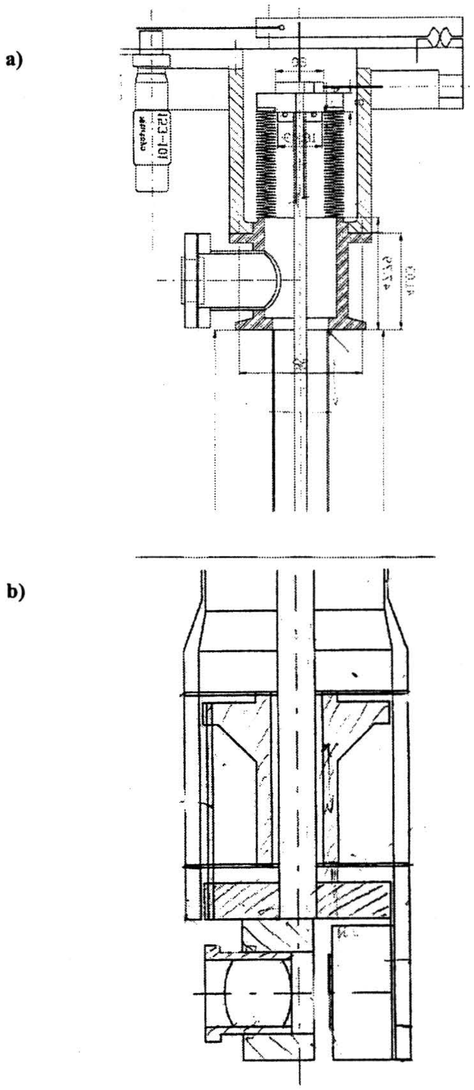

Figure 3.8: *a) The spring based manipulation system, which can be externally scanned, is connected with the lens. b) Externally scannable lens just in front of the sample holder.*

The aspheric lens is mounted on the insert just in front of the sample for stability. The raw focussing is done manually outside the cryostat. Three micrometer screws are attached to the lens, to be able to steer the laser spot over the sample with a conveyance of 30:1. Two micrometer screws are for scanning over the sample and a third one for the fine adjustment for focussing of the lens. This enables us to scan the externally in all three directions with a precision of 0.1 μm using the spring-based manipulation system. The maximum adjustable distance of the aspheric lens inside the cryostat is 300 μm.

3.5 Micro-Photoluminescence Experiments (Non-resonant excitation)

The characteristic feature of μ-PL is that the excitation spot size is in the order of microns. In this way we are able to excite only a small number of dots and can observe, what is to be most likely in our case, a homogeneous set of dots. Due to the small spot size, high excitation density can be achieved. Measurements are carried out with excitation densities in the range of 10^0 - 10^4 W cm^{-2}. All three laser systems are suitable to perform μ-PL. The monochromator is used in subtractive mode with a spectral resolution of 80 μeV. The condition of obtaining clear peak(s)in the PL spectrum, which are characteristic of systems with a discrete energy levels, is to avoid thermal broadening. Therefore the measurement are taken at 5K, so that the condition $k_BT \ll \delta$ (δ is the energy separation of neighboring energy levels) is satisfied. Furthermore, at low temperatures phonons are less probable to dephase with excitons, which also results in a more clear PL spectrum. First the PL intensity of the GaAs QW is optimised by the mirrors and the lenses in front of the monochromator. The correction for the astigmatism is checked and adjusted if needed. Subsequently the emitted PL of the QDs, displayed on either the CCD camera or the PMT, is also optimised by the mirrors and lenses in front of the monochromator. The principle of PL experiments is presented in Fig. 3.9. A laser beam of appropriate wavelength excites the electrons from the valence band to the conduction band and creates electron-hole pairs ($E_{in} \rightarrow e + h$). These pairs can be excited into the discrete levels of the dot, into the two dimensional quantum well or into the bulk semiconductor continuum. The wavelength of the excitation source is in most cases $\lambda \leq 700$ nm and the electron-hole pairs (excitons) are created above the energy levels of the dots, in the GaAs QW. A fraction of the generated particles are captured into the QD and relax non-radiatively to the ground state or into weakly excited states of the QD. Finally, the electron-hole pairs confined in the QD recombine, emitting photons, which are then detected ($e + h \rightarrow E_{out}$).

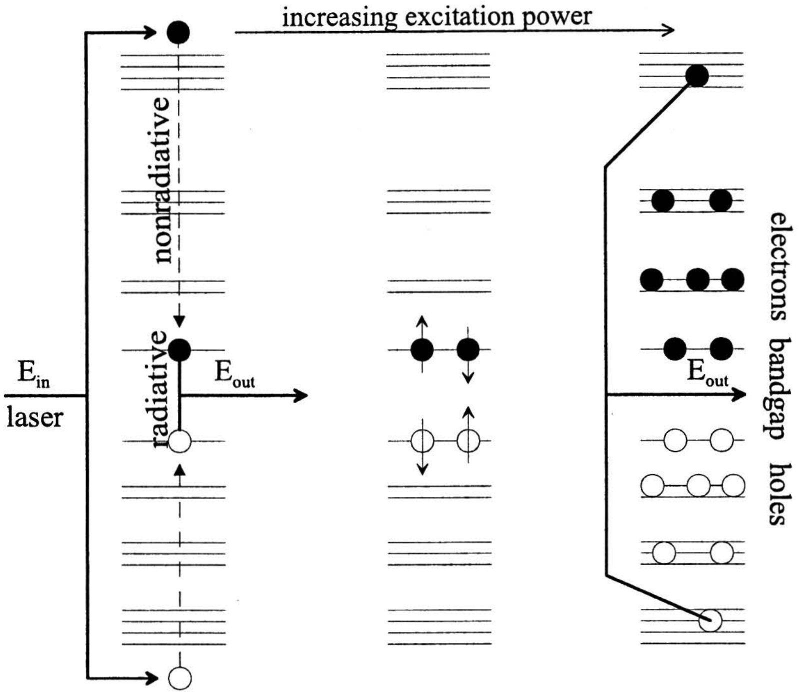

Figure 3.9: *Photoluminescence experiment: measurement of the intensity of the outgoing beam* E_{out} *as function of the wavelength.*

Depending on the exciton creation rate, which is related to the excitation density of the sample two situations are possible:
(i) The number of created excitons is so small that at most a single exciton is confined at a time in each dot (each confined exciton recombines before the capture of the next one during its recombination lifetime). When the relaxation rate is higher than the recombination rate, almost all excitons relax to the ground state before recombination, and a single peak will dominate the PL spectrum. The reason for the occurrence of higher-energy peaks in the PL spectrum may be the presence of excited states in the energy level system, for which the characteristic relaxation time is larger than the recombination lifetime, as discussed in 2.5.

(ii) The carrier capture rate into the QDs is larger than the recombination rate. In this case the number of created pairs is large enough to reach the state of quasi-equilibrium, in which the dot is populated with a number (N) of bound excitons. In such a case, the recombination from the initial (ground) state of N excitons is possible either to the final ground state or to final excited state of $N-1$ excitons. Due to Pauli's exclusion principle, some of the particles occupy higher-energy levels and therefore multi-excitonic spectra can be observed.

For identical excitation density, in pulsed excitation all carriers will recombine, before the next excitation pulse. The last recombination will most likely be the 1X $\longrightarrow$ vacuum recombination, when only one exciton is still remaining in the QD. So in a pulsed excitation PL experiment, the single exciton recombination peak is expected to occur always and thus be dominantly present in the PL spectrum.

3.5.1 Resonant Photoluminescence (RPL)

The excitation energy in RPL is in resonance with the higher confined energy levels of the QDs. The excitation wavelength for RPL is $\lambda > 700$ nm for our measurements. The carriers can relax to the lower energy levels and the emitted PL from the these levels will be detected. By exciting higher energy levels and observing the emitted PL one can get more insight in the QD characteristics. To make sure only one energy level is excited, a narrow linewidth for the excitation beam is required. Knowing the pulsewidth of the laser it is possible to calculate the linewidth of the excitation beam, assuming transform limited pulses, from the uncertainty principle ($\triangle E \triangle t \geq \hbar/2$). When using the Ti:sapphire laser system in cw mode ($\triangle t$ can be considered infinitive), the linewidth ($\triangle E$) of the excitation beam is a few meV, which is considered sufficient narrow for exciting only one energy level. The excitation density will in general need to be higher because of the lower absorption probability for the QDs. The measured spectra however will have a lower background with respect to the non-resonant PL due to the absence of GaAs QW related PL. Because of the lower absorption coefficient of the QDs compared to the QW also the amount of excited carriers is less. When less electron-hole pairs are created the probability of Auger scattering (and thus dephasing) is lower, resulting in less broadening of the peaks. A narrow linewidth of the excitation beam enables the possibility to do PhotoLuminescence Excitation (PLE). Apart from high excitation densities to observe excited states of the QD, also PLE can be used. PLE is based on an absorption depending measurement technique. The energy of the excitation beam E_{in} is varied and only the emitted PL is detected on a fixed wavelength. The intensity of the detected system is related to the number of electron-hole pairs excited at a given energy E_{in}. This is because the number of electron-hole pairs that relax to the state from which recombination is detected depends on the total number of created pairs. On the other hand, the absorption probability is proportional the joint (optical) density of states of the electron-hole pair. Hence, a peak in the PLE-spectrum corresponds to a peak in the optical density of states, which in the QD case translate to a discrete energy level diagram.

3.5.2 Time Resolved Photoluminescence (TRPL)

To obtain experimental evidence for possible long relaxation times, time resolved measurements are required [23]. The time dependent properties of each individual peak can be analysed by fixing the monochannel detector at the center of a PL-peak. The PMT is replaced by a fast Hamamatsu R3809U-51 microchannel plate PMT. Time Correlated Single Photon Counting (TCSPC) is used for TRPL. A pulsed laser system is needed to generate a "start" and "stop" signal. The pulsewidth of the modelocked Ti:sapphire laser system is 150 fs which results in a linewidth of approximately 30 meV. The repetition rate of the laser is 78 MHz. The excitation pulse triggers the fast photodiode (j), see Fig. (3.6), which is electronically delayed and will eventually act as a stop signal for the time dependent measurement. It should be mentioned that the number of photons per pulse is larger than the number of emitted photons. The emitted PL is detected by the microchannel plate and the first emitted photon acts as the start signal for the time dependent measurements. The microchannel plate is connected to a 1-GHz amplifier and timing discriminator, which is optimised for use with millivolt signals produced by microchannel plate detectors. The timing discriminator output logic pulse can be transmitted over much longer cables to a time to pulse height analyser, which is subsequently connected to a multichannel analyser (MCA) without compromising the picosecond time resolution. The electronic delay of the measurement equipment is calibrated with a timing calibration and the time resolution is measured using the 150 fs laser pulse and is of the order of 90 ps. The excitation can be done in the bulk or GaAs QW or close to (near resonant PL) or in (RPL) resonance with the quantised levels of the QDs. However due to the broad laser line in resonant excitation multiple energy levels can be excited.

Chapter 4

Micro-Photoluminescence Experiments

4.1 Introduction

Optical measurements allow to probe the electronic structure of a dot in detail, which will be required for a full understanding of QD structures. The number of lines increases with increasing excitation density, which is assumed to correlate with an increasing number of charge carriers in the dot. Optical studies of semiconductor QDs might open new possibilities for investigating Coulomb interactions in multiparticle states consisting of electrons, holes and excitons. In this chapter, high spectral resolution photoluminescence is carried out and discussed.

4.2 Previous Results of PL on QDs

The confined nature of the single-particle states in QDs has been shown by various techniques of optical spectroscopy. Multiparticle effects are of importance in a variety of aspects of the linear and nonlinear optical properties of semiconductor quantum structures. The number of charge carriers in QDs correlates with excitation power. Thus by varying the excitation power density, the number of charge carriers in the QDs can be influenced. The formation of multiparticle complexes in QDs is determined by the strong Coulomb interactions among carriers. The interplay of these effects can cause new collective phenomena. A well-known example of such a complex is the biexciton. Biexcitons in QDs have been subject of a number of investigations [6, 30, 31]. A systematic increase of the ground state biexciton binding energy with decreasing dot size was found by Bayer *et al.* [30]. Landin *et al.* however observed the recombination energy of the biexciton below as well as above the single exciton peak. In a quantum well a biexciton is formed by molecule-like attraction, making the biexciton emission energy lower that the single exciton emission. In a quantum dot the electron and hole wave functions are primarily determined by the strong confining potential. The charge distribution resulting from those confined wave functions is determining the Coulomb energy, depending on the relative strengths of the electron-electron, hole-hole and electron-hole interactions. In general, it is believed that the biexciton binding energy is of the order of magnitude of 2 - 5 meV. It is also found in literature that the luminescence lines of the biexciton recombinations grow superlinearly approximately proportional to the square of the excitation density [6, 7].

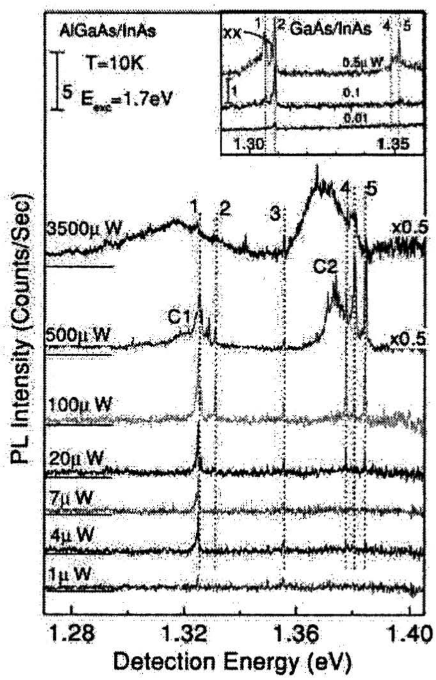

Figure 4.1: *Single SAQD PL spectra at various cw excitation powers [11]. The exciton is labelled 2, the biexciton as 1 and 3 and higher represent excited states. The inset contains similar spectra from SAQD sample without aluminium.*

At even higher excitation densities carriers will also fill higher energy levels with multiparticle complexes and are able to recombine from excited states. A typical PL spectra is shown in Fig. 4.1. The PL spectra are composed out of groups of emission lines, with a few characteristic spectral lines in each group. The rate at which the intensity of each emission line grows with excitation power is different. This behavior has been observed in several multi-excitonic recombination spectra. At low excitation densities, emission from the ground state is observed [7, 11, 18]. The ground state can be occupied by not more than two excitons, resulting in a group of peaks at the low energy side. Increasing excitation densities results in complete ground state filling and saturates emission. Simultaneously, emission from the second energy level appears, resulting in a group of lines at higher energy. According to the model the lowest energy peak (line number 1) should appear only when the number of excitons exceeds two. The first peak observed by Dekel *et al.* however is the lowest energy peak, which is designated as the biexciton recombination, instead of the expected single exciton recombination, see Fig. 4.1. This discrepancy is explained by Dekel *et al.* in terms of nonradiative recombination channels which are very efficient at low excitation densities and quickly saturate at higher excitation densities. Such nonradiative recombination channels are known to be the result of aluminium content in the barrier layers. The quick saturation of these non-radiative recombination channels at higher excitation density is, in our view quite surprising. Therefore GaAs QDs embedded in InAs are also measured for comparison as can be seen in the inset. In the absence of the nonradiative decay channels, associated with aluminium, the single exciton (2) and biexciton (XX) lines are clearly observed in these spectra already at extremely low excitation powers. Emission lines of electrons and holes that occupy excited confined energy level have been reported, however these lines are still not completely understood in a coherent picture which agrees with experimental observation of different authors. Therefore it is important to get an insight in the electronic structure, the characteristic role of energy level filling and carrier relaxation of QDs.

4.3 Experimental Observations

The sample was lightly glued on a coldfinger with characteristic direction of the sample as close as possible in the directions of the micrometer screws. The emitted PL of the GaAs QW is a broad peak around 695 nm (1.78 eV) and the PL lines of the QDs near 765 nm

(1.62 eV) [4], see Fig. 4.2.

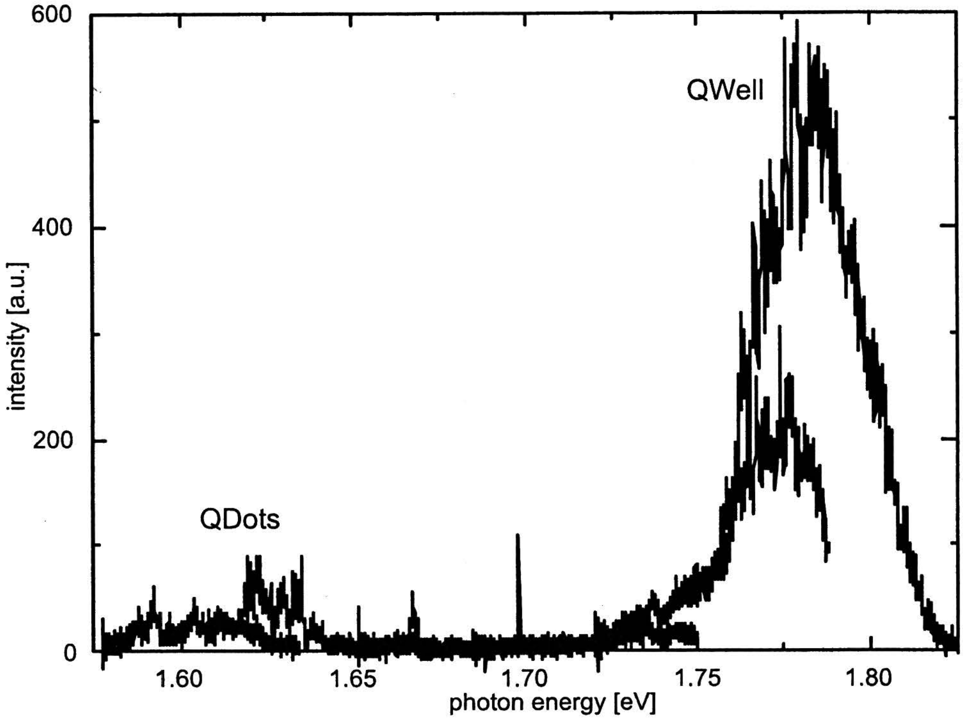

Figure 4.2: *Micro-PL spectra taken at 5 K at different wavelength positions of the monochromator.*

The QW is used as reference and for optimising the throughput of the monochromator. Photoluminescence measurements are carried out with different excitation densities. The excitation power is attenuated by Neutral Density (ND) filters in series with a rotating gradient ND filter. These filters are selected in order to have minimum spatial displacement of the excitation beam, since any such displacement also moves the excitation spot away from the QDs under study. While scanning over the sample, abrupt appearance and disappearance of PL peaks is observed. This is strong evidence for the local homogeneity of the QDs. The measured PL spectra are shown in Fig. 4.3.

The sample is excited with the dye laser at 585 nm (2.13 eV) with a repetition rate of 78 MHz and a pulsewidth of approximately 1 ps. The emitted PL is dispersed by the monochromator in subtractive mode. The spectral resolution in subtractive mode, see table

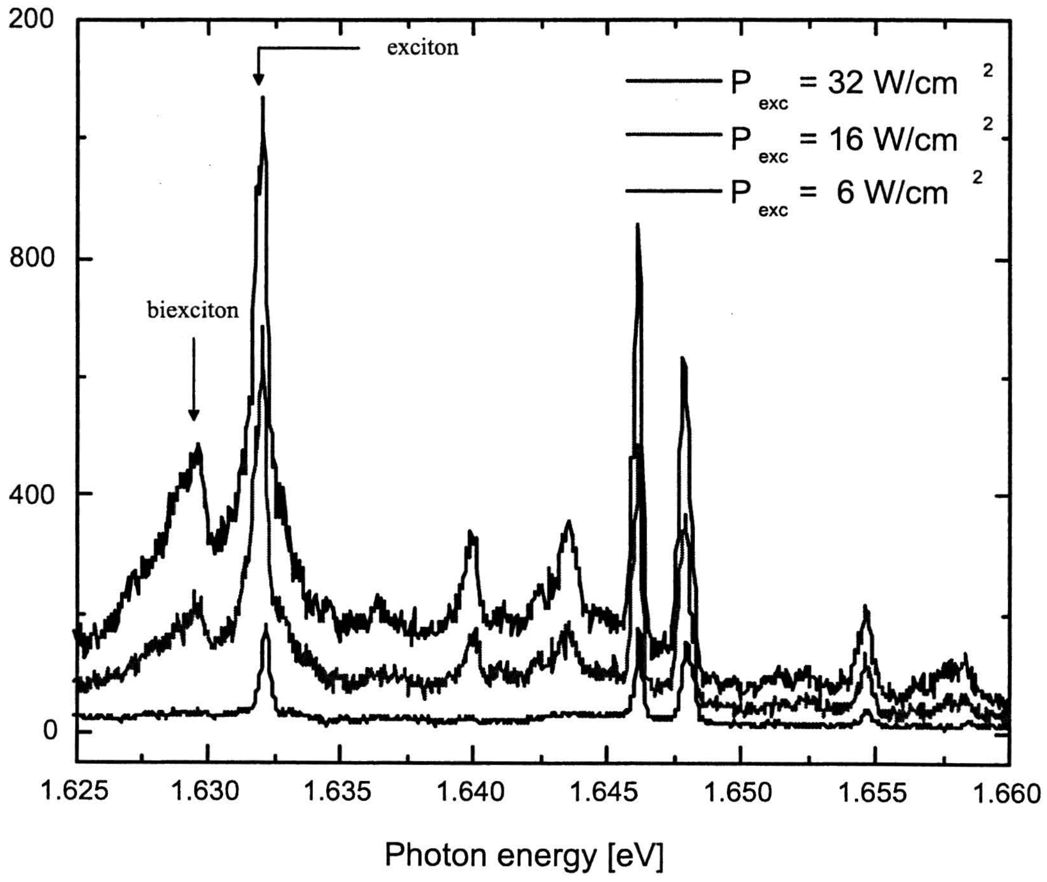

Figure 4.3: *Photoluminescence spectra of GaAs QDs for different excitation densities.*

3.2, is 80 μeV. The integration time was 1 minute except for the lowest excitation density where it was 15 minutes. The intensity of the lowest excitation density is normalised to 1 minute. Figure 4.3 shows three distinct peaks at the lowest excitation density developing in a more complex PL spectra with increasing excitation density. The spectra features a great resemblance with previous observed PL spectra on single QDs reported in literature. We however want to emphasize that we observe QD-arrays with approximately 25 QDs within our excitation spot. Assuming non-homogeneous QDs, the pronounced measured PL peaks originate from QDs with different dimensions. Figure 4.3 shows three pronounced peaks at 1.6320, 1.6461 and 1.6479 eV respectively. Those three PL peaks might originate from single ground state exciton confined in a QD with different dimensions. The QD dimensions can be determined by varying them, so that the recombination energy will become 1.6320 or 1.6461 eV respectively. If the PL at that energy is emitted by a single ground state exciton confined in a QD, the dimension of such a QD emitting an photon at 1.6320 or 1.6461 eV would be approximately $36 \times 39 \times 7.40$ nm^3 or $32 \times 34 \times 7.06$ nm^3, respectively. That would mean that the QD dimensions would vary about 10 % within 2 μm, which could be possible. The same applies for the PL peak at 1.6479 eV as well as for the pronounced PL peaks measured in Fig. 4.5b. However based on our measurements we assume we are dealing with a set of *homogeneous* QDs with no size fluctuations on the length scale of the laser spot (≈ 2 μm), as will be discussed in the next paragraph.
The strong PL peak at approximately 1.632 eV is considered to be the single exciton peak. The feature at the low energy side is assumed to be the biexciton peak. The peaks at higher photon energies are assumed to be excited exciton recombinations, which will be discussed in the next paragraph. The photon energy difference between the single exciton and biexciton is 2.5 meV, which is in good agreement with previously reported results. Taking a closer look at the evolution of the peak intensities of the exciton and biexciton, results in Fig. 4.4.

The different behaviors of the single exciton and biexciton with increasing excitation density are shown. The PL peak of the single exciton grows linear with increasing excitation density up to a certain density where saturation effects become dominant. The biexciton intensity differs from the linear dependency, shown by the drawn line, see Fig. 4.4. The intensity of the biexciton peak is growing superlinear with increasing excitation density. Once again this behavior is exhibited until saturation effects become dominant. This behavior is observed multiple times at various positions at the sample. Therefore it is

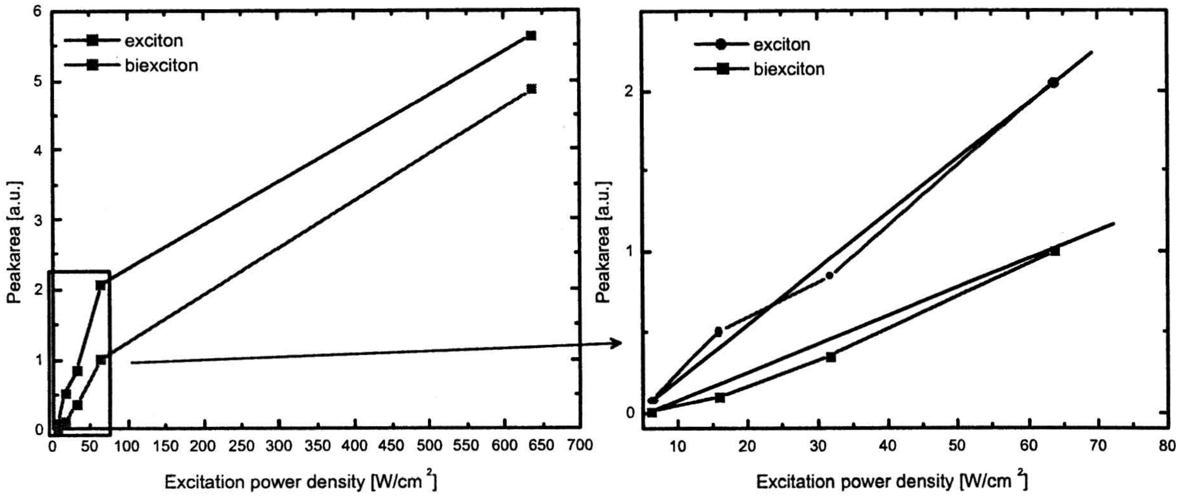

Figure 4.4: *Evolution of the peak intensity as a function of the excitation density. The lines drawn represent linear dependency between peak intensity and excitation density.*

likely to assume that biexcitons exhibit a superlinear dependency with increasing excitation density.

Subsequently, PL measurements were carried out in order to make a comparison between excitation with the HeNe (cw) laser system with excitation at 633 nm in the QW and the Ti:sapphire mode locked laser at 746 nm, exciting only in the QDs, at identical positions at the sample. Note that these measurements are performed at a different position on the sample with respect to the spectra measured in Fig. 4.3. The difference between excitation in the quantum well and quantum dot can be seen in Fig. 4.5a. Excitation in the QDs results in a cleaner spectrum with the peaks more distinctively visible. In this situation the detection region is close to the energy of the excitation beam, which causes the increase in intensity at higher photon energies. PL measurements for different excitation densities are carried out for excitation at 746 nm as well, see Fig. 4.5b. Higher excitation densities are needed because of the lower absorption of the QDs compared with excitation in the QW. Once again spectra similar as discussed before are observed. The full width at half maximum (FWHM) of the dominant peak at 1.6194 eV, which is considered to be the single exciton peak, is approximately 170 μeV. The FWHM of the single exciton peak, results in a dephasing time of ≥ 2 ps. The observed spectra for excitation at 746 nm are an excellent example to show the high amount of regularity of the position of the different PL peaks. Exciting in the QDs, avoids QW related PL, leading to better information about the optical properties of QDs.

4.3.1 QD homogeneity

In section 3.2 it is assumed that we are dealing with a set of *homogeneous* QDs within an one dimensional array. Careful analysis of the numerous PL measurement which have been carried out, yield a number of strong indications for the local homogeneity of the QDs in the arrays. These indications are: (i) Upon scanning the excitation spot along the QD-array, the abrupt and simultaneous appearance and disappearance of successive multi-excitonic features with very sharp peaks (< 0.2 meV) are observed. (ii) The QD emission peaks show a small asymmetric broadening, as already reported by Nötzel *et al.* [4], which indicates small size fluctuations between the homogeneous QDs. (iii) The excitation density dependent measurements show the appearance of new peaks, with identical peak characteristics, with increasing intensity indicating a multi-excitonic spectrum instead of PL lines originating from dots with different dimensions. (iv) After analysis of many measured PL spectra, the spectra do not show randomly distributed peaks along the energy axis; the positions of the different peaks are strongly correlated. (v) Our exciton lifetime measurements using TCSPC and pulsed excitation show that only the ground state exciton has a delayed risetime [11, 32] at higher excitation density, see Fig. 4.6 . Due to practical reasons these measurements could not be performed on the identical positions at the sample where the previous spectra are measured. Nevertheless, the lifetime measurements are performed on PL peaks which display a high analogy with the previously observed spectra. Such a delayed risetime is typical for the ground state exciton since the ground state exciton recombination line becomes visible only after the recombination of all other excitons in multi-excitonic complexes.

Taking into account these indications, we thus interpret the μ-PL spectra as multi-excitonic spectra from locally homogeneous QD-arrays. On macroscopic distances along the QD-array however, the μ-PL spectra can strongly vary, indicating that the QD dimensions and excited state degeneracy, determined by the symmetry along $[01\bar{1}]$ and $[\bar{2}33]$ vary substantially with macroscopic position.

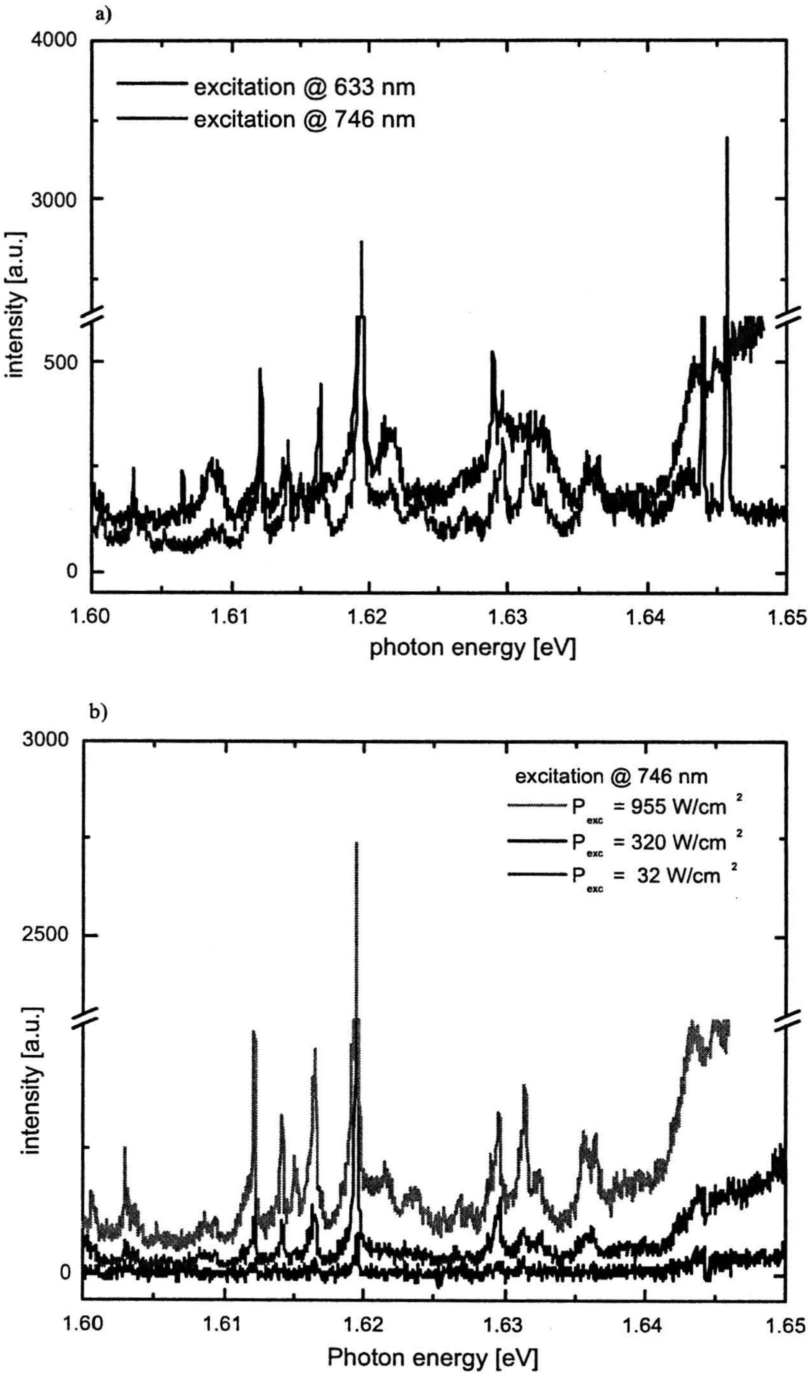

Figure 4.5: *a) Comparison of PL with excitation at 633 nm (cw HeNe laser) and excitation at 746 nm (Ti:sapphire mode locked laser)with an excitation density of 160 and 960 W/cm*^{2} *respectively. The two sharp lines at about 1.645 eV are laser lines from the He-Ne laser. b) PL spectra with excitation at 746 nm (Ti:sapphire mode locked laser) for different excitation densities.*

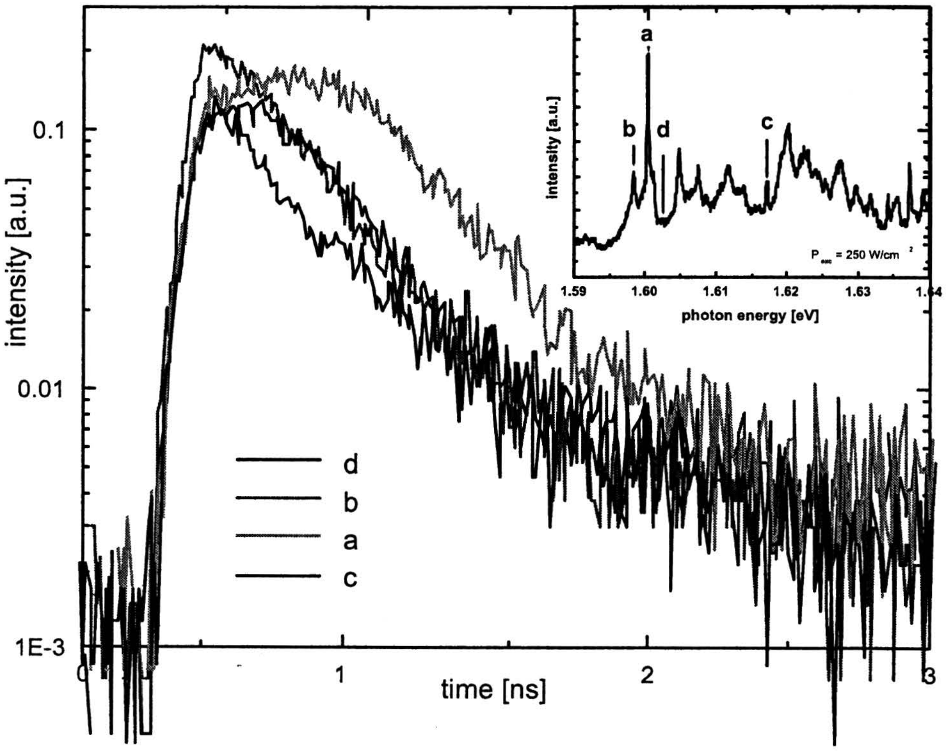

Figure 4.6: *Time resolved PL measurements on a spectra with high analogy with previously observed spectra.*

4.4 Interpretation of the observed PL spectra

4.4.1 Assignment of the excited single exciton lines

For the spectrum observed in Fig. 4.3, we observe the ground state (11) single exciton (1X) at 1.6320 eV and a biexciton (2X) line at 1.6295 eV, corresponding to a biexciton binding energy of 2.5 meV. In addition we observe sharp peaks at 1.6461 and 1.6479 eV, which we attribute to the (12) and (21) single excited exciton, since these peaks emerge already at low excitation density. Recombination of carriers is only allowed for carriers which occupy the same confinement level, since conservation of the quantum numbers $n_i^e = n_i^h$ is required. Therefore the positions of the excited single exciton recombinations correspond to the confined energy levels corrected by the Coulomb interaction energies, which can be calculated by equations (2.12) and (2.16), see appendix for exact values. By varying the dimensions of the QD the corrected energy levels have to coincide with the recombination energies. Doing so for the spectrum measured in Fig. 4.3 QD dimensions of 36.2 x 38.9 x 7.40 nm^3 are obtained for electron and hole effective masses equal to $m_e^* = 0.067 m_e^0$ and $m_h^* = 0.5 m_e^0$. The obtained dimensions of the QD are in reasonable agreement with the dimensions measured by AFM. The fact that the two sharp peaks at 1.6461 and 1.6479 eV match with the (12) and (21) excited exciton levels of a QD of these dimensions, is a strong indication for our assignment. The same procedure is done for the spectra shown in Fig. 4.5 which results in QD dimensions of 36.5 x 35.5 x 7.84 nm^3, see also appendix. It should be stressed that the assignment of these two lines is not yet final. We will however show that this provisional assignment allows us to eventually fit multiple exciton (3X → 2X and 4X → 3X) and excited biexciton features, which emerge at higher excitation densities, with a small number of additional fitting parameters.

4.4.2 Identification of the observed recombination lines

Depending on whether carriers relax to their lowest possible energy state before they recombine (A), or whether they recombine before they relax (B), two different ways of filling the QD are distinguishable. The first situation (A) greatly simplifies the spectrum, since the number of possible initial states before recombination is reduced. In a system where the particle relaxation time is longer (B) than the exciton recombination time [12, 7], additional recombination are possible and extra PL peaks can occur in the PL spectrum. We focus on the Coulomb and exchange interaction [21] that arise between the carrier occupying the single QD by applying a Hartree Fock approximation treating the QD confinement levels with a simple particle-in-a-box model, as described in chapter 2. The energy of an exciton in the ground state is given by equation (2.17) and the biexciton energy is expressed in equation (2.18). If the single exciton (1X) recombines, the final state is the vacuum (v) state: a single line appears in the spectrum. Upon recombination of a biexciton (2X), the 1X is the only allowed final state, also contributing a single line to the PL spectrum, see Fig. 4.7. The recombination energy of a certain state in a PL experiment can be calculated by the difference between the final state energy and the initial state energy:

$$E_{PL} = E_{initial} - E_{final}.$$

The band gap energy E_g of GaAs at 5 K, which is $E_g = 1.5190$ eV, has to be added for the correct value in the PL spectrum. Applying this to the case of biexciton recombination, results in:

$$\begin{aligned} E^0_{PL,2X} = E_g + E_{2X} - E_{1X} = \\ E_g + E_{1X} + V_c^{11/11}, \end{aligned}$$

with $V_c^{11/11}$ known as the biexciton binding energy, see Fig. 2.4 and equation (2.18). Additional PL lines can be constructed by allowing recombination of single excitons from the QD's first (12) and second (21) excited energy levels to vacuum, as discussed in 4.4.1, at energies E_{1X^*} and $\mathrm{E}_{1X^{**}}$, see table 4.1. The first excited biexciton states, have one electron in (11) energy level and another in (12) or (21) energy level, are represented by $2\mathrm{X}^{*s}$ or $2\mathrm{X}^{*t}$ and $2\mathrm{X}^{**s}$ and $2\mathrm{X}^{**t}$, respectively. In the excited biexciton configuration, either the exciton in the (11) or in the (12) can recombine, resulting in four different recombinations: $2\mathrm{X}^{*s} \rightarrow 1\mathrm{X}$, $2\mathrm{X}^{*s} \rightarrow 1\mathrm{X}^*$, $2\mathrm{X}^{*t} \rightarrow 1\mathrm{X}$, $2\mathrm{X}^{*s} \rightarrow 1\mathrm{X}^*$, shown in Fig. 4.7. Identical recombination transitions are possible for the $2\mathrm{X}^{**t}$ and $2\mathrm{X}^{**s}$ configurations. Table 4.1 displays an overview of the possible transitions with up to four excitons.

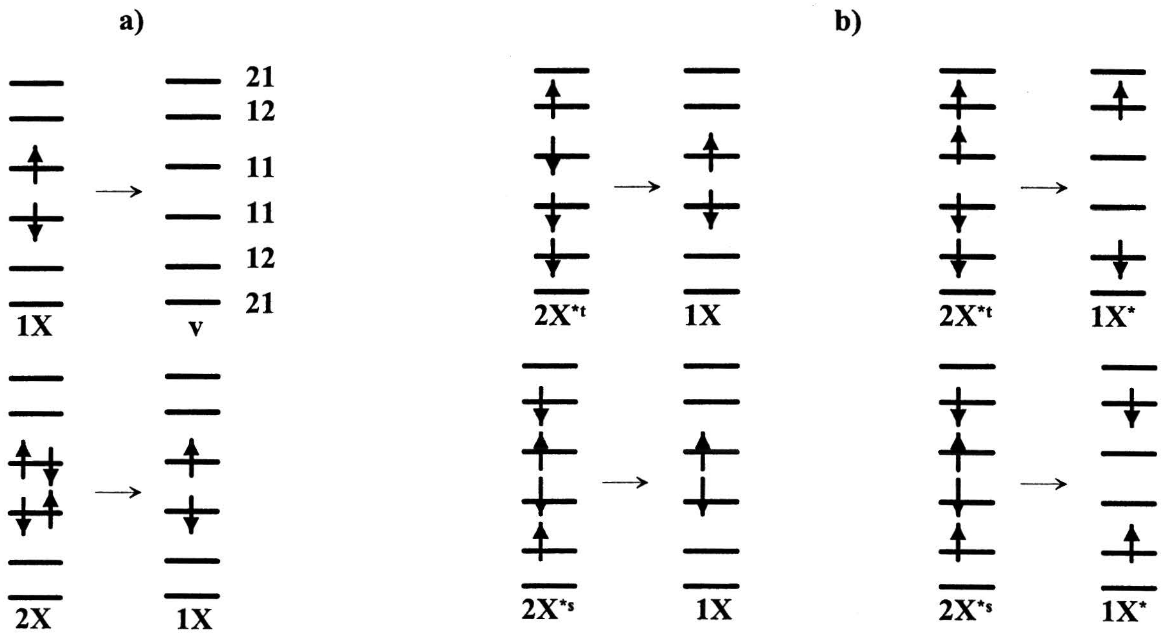

Figure 4.7: *a) The ground state* $1X \rightarrow v$ *and biexciton* $2X \rightarrow 1X$ *recombinations are shown. The electron and hole ground state, first and second excited states are indicated with (11), (12) and (21) respectively. Vertical arrows show the electron and hole spin alignment. b) Various excited biexciton to exciton transitions. Superscripts 's'and 't' indicate the singlet and triplet configuration.*

Table 4.1: *The various transitions from the three lowest energy levels, occupied with up to four excitons. Also shown are the PL energies, expressed with regard to other tabulated PL lines and with appropriate Coulomb and exchange energy terms. The labels 'a' through 'p' identify the lines with respect to the figures.*

PL transition	PL energy	label (ICR)	label (ISR)
1X → v	E_{1X}	(a)	(a)
$1X^{*}$ → v	$E_{1X^{*}}$	(c)	(c)
$1X^{**}$ → v	$E_{1X^{**}}$	(d)	(d)
2X → 1X	$E_{1X} - V_c^{11/11}$	(b)	(b)
$2X^{*s}$ → $1X^{*}$	$E_{1X} - V_c^{11/12}$	(e)	(m)
$2X^{*s}$ → 1X	$E_{1X^{*}} - V_c^{11/12}$	(f)	(n)
$2X^{*t}$ → $1X^{*}$	$E_{1X} - V_c^{11/12} - V_x^{11/12}$	(g)	(e)
$2X^{*t}$ → 1X	$E_{1X^{*}} - V_c^{11/12} - V_x^{11/12}$	(h)	(f)
$2X^{**s}$ → $1X^{**}$	$E_{1X} - V_c^{11/21}$	(i)	(o)
$2X^{**s}$ → 1X	$E_{1X^{**}} - V_c^{11/21}$	(j)	(p)
$2X^{**t}$ → $1X^{**}$	$E_{1X} - V_c^{11/21} - V_x^{11/21}$	(k)	(g)
$2X^{**t}$ → 1X	$E_{1X^{**}} - V_c^{11/21} - V_x^{11/21}$	(l)	(h)
3X → 2X	$E_{1X^{*}} - 2V_c^{11/12} - V_x^{11/12}$	(m)	(i)
3X → $2X^{*t}$	$E_{2X\rightarrow 1X} - V_c^{11/12}$	(n)	(j)
3X → $2X^{*s}$	$E_{2X\rightarrow 1X} - V_c^{11/12} - V_x^{11/12}$	(o)	(k)
4X → 3X	$E_{1X^{*}} - 2V_c^{11/12} - V_x^{11/12} - V_c^{12/12}$	(p)	(l)

Identification of PL transitions in the measured spectrum Fig. 4.8 can be done by varying the various energy terms as fitting parameters. The 1X → vacuum and 2X → recombination lines are used to fit E_{1X} and $V_c^{11/11}$, while the two excited single exciton transitions are used to fit $E_{1X^{*}}$ and $E_{1X^{*}}$. Having fit these four lines, 11 other peaks in the spectrum ('e' through 'o') can be fitted with only 4 additional parameters, being $V_c^{11/12}$, $V_x^{11/12}$, $V_c^{11/21}$ and $V_x^{11/21}$. The 4X → 3X (line 'p') recombination requires one additional free parameter $V_c^{12/12}$. The most important features of the measured spectrum can be identified by choosing the proper values for the fitting parameters, see Fig. 4.8 and table 4.2. The fitting method used for Fig. 4.8 will be called "incomplete carrier relaxation"

(ICR). Having in mind the list of possible transitions of 4.1, groups of lines can be fitted by varying the different Coulomb and exchange contributions in order to obtain a high quality fit. It should be mentioned that line (o) lies outside the energy range of the measurements. Due to the fact that only four excitons and the first three energy levels are considered, we are unable to identify the features above 1.65 eV. Calculations indicate that the (22) energy level is to be expected at an energy of about 1.66 eV.

However, based on spin relaxation related results in literature [12, 33, 34], singlet states are expected to have a lower probability to recombine before they relax than triplet states. Due to the fact that triplet configurations need a spin-flip [33] process before they can relax to a lower energy configuration. This spin-flip process in combination with relaxation will require more time, hence recombination before relaxation to a lower energy state will have a higher probability. Therefore, it is more likely to observe peaks from triplet states in the PL spectrum. By taken into account these considerations, we will again try to explain the most important features in the measured spectrum, see Fig. 4.9. The method of fitting in this way will be called "incomplete spin relaxation" (ISR). The fitted PL lines for the singlet states are displayed at the bottom part of the figure, representing a lower probability. In the appendix all possible configurations and transitions are listed together with extensive fit to the measured spectrum for the two different fits.

Again by fixing the transitions of the PL peaks 'a' through 'd' and varying four additional fitting parameters an adequate fit of the measured spectrum can be made. Comparing the resulting values of the two different manners of fitting the measured spectrum of Fig. 4.3, leads to table 4.2. The biexciton binding energy is chosen to be the same for the two fits.

Notice that our simple QD model predicts a zero value for the biexciton binding energy and other biexciton Coulomb terms. The Coulomb interactions that compose the biexciton binding energy exactly cancel in a QD with infinitely high barriers, resulting in identical electron and hole envelope functions and thus a zero net charge distribution. Furthermore, all Coulomb energy terms are composed out of four Coulomb terms of values in the order of 10 meV. In different confinement limits, deviations may come from asymmetry of interactions. Depending on whether the electron-hole attraction is weaker than or equal to the electron-electron and hole-hole repulsion, slight deviations may occur by adding and subtracting these values, leading to a contribution in the biexciton binding energy. Such a cancellation does not occur for the exchange term. A slight deviations in the exchange

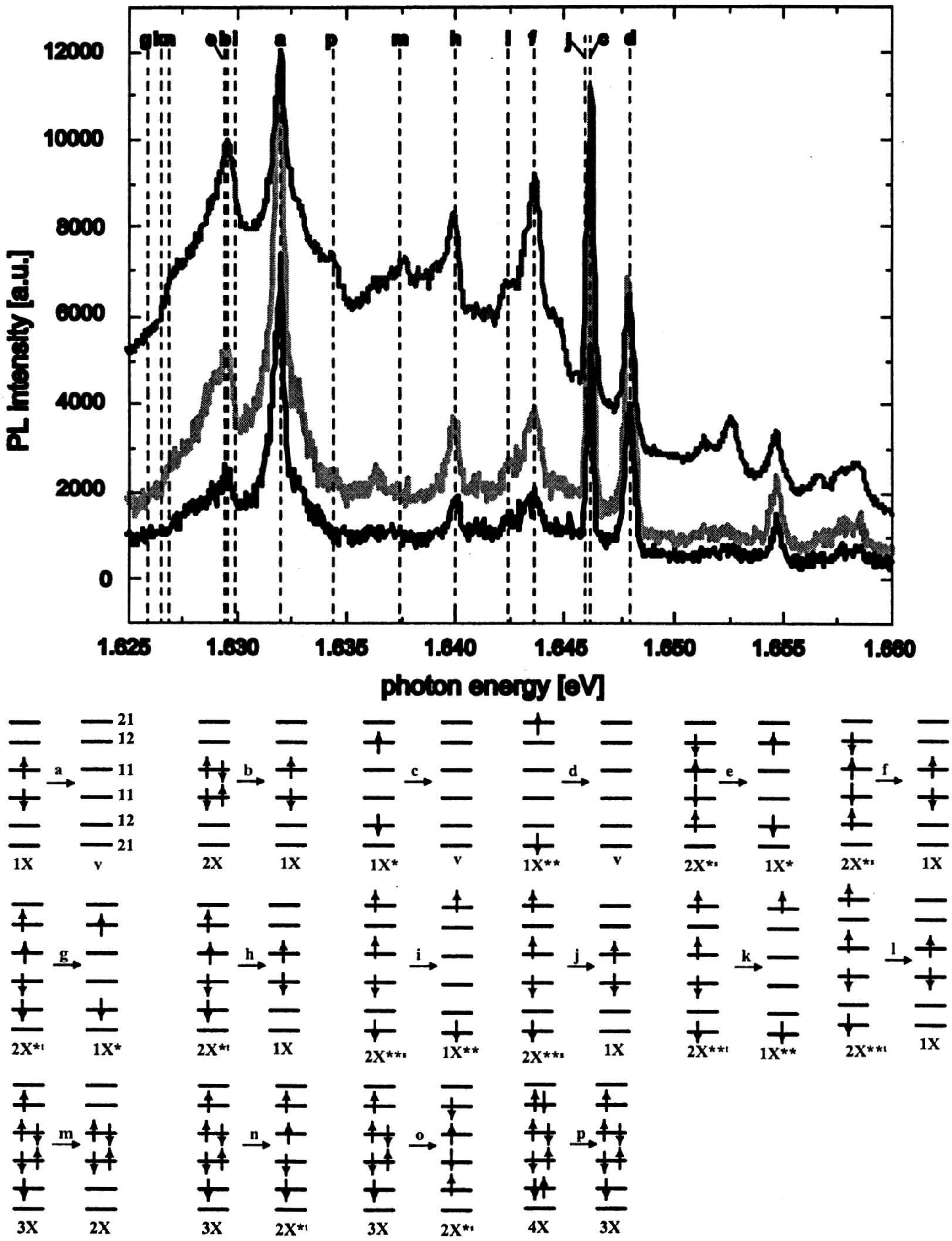

Figure 4.8: *Micro-PL spectra, measured at identical positions on the sample taken at 16, 32 and 640 W/cm*^{2}*. Note that the x-axis has an offset between the highest excitation density and the other two excitation densities. The various transitions from the three lowest energy levels are shown corresponding to the labels in Table 4.1.*

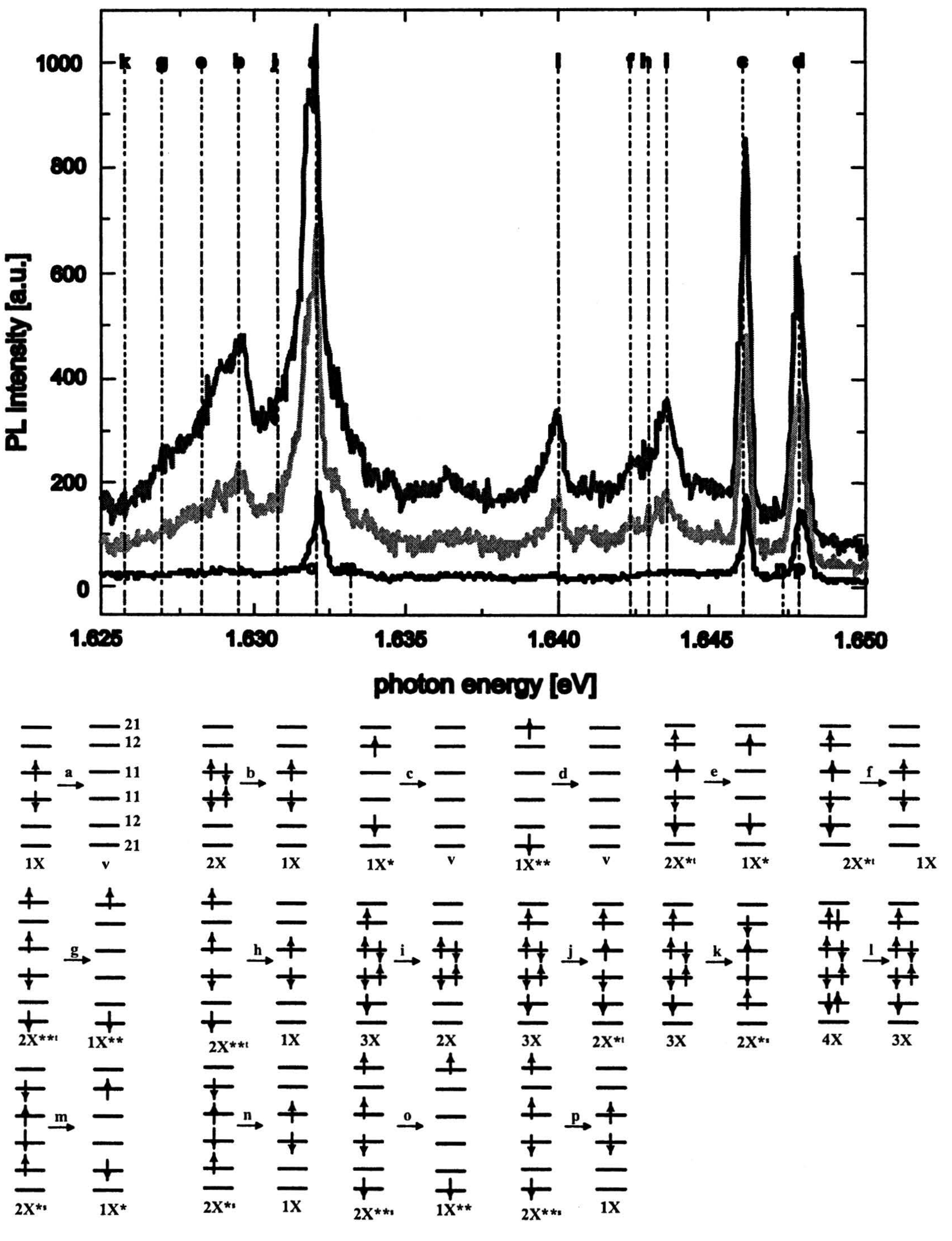

Figure 4.9: *Micro-PL spectra, measured at identical positions on the sample taken at 6.5, 16 and 32 W/cm^2. The various transitions from the three lowest energy levels are shown corresponding to the labels in Table 4.1.*

Table 4.2: *The extracted values for the various interaction terms of the two different fitting methods for Fig. 4.3. The values shown are in meV.*

interaction term	incomplete carrier relaxation	incomplete spin relaxation
$V_c^{11/11}$	-2.5	-2.5
$V_c^{11/12}$	-2.6	1.2
$V_c^{11/21}$	-2.0	0.5
$V_c^{12/12}$	-3.0	-3.6
$V_x^{11/12}$	-3.5	-4.9
$V_x^{11/21}$	-3.5	-4.8

energy values is obtained in comparison with the theoretical calculated value of - 7.0 meV. Once again this is caused by the simplicity of our model, which is based on ideal QDs which have impenetrable walls. In practice, the wavefunctions of the carriers will penetrate into the barrier and hence the exchange energy will decrease due to the decrease in overlap of the wavefunction from different energy levels.

Nevertheless, it appears that by choosing four lines and varying the values for the interaction energy terms, two high quality fits can be obtained. However, it should be mentioned that by allowing the carriers to relax to the lowest possible energy level, no high-quality fit of the spectrum can be obtained. These observations and corresponding fits indicate the presence of a phonon bottleneck in these strain free QDs.

These fitting methods can be applied to the measured spectra of Fig. 4.5b for checking the accuracy of the two fitting methods. Notice that these measurements are carried out with excitation using the mode lock Ti:sapphire laser system at 746 nm. As already displayed in Fig. 4.5a, fine distinction are noticeable between exciting in the QW and QD. Applying the incomplete carrier relaxation method for the measurements of Fig. 4.5b, results in Fig. 4.10.

The quality of the fit is not as good as it is for the measured spectra of Fig. 4.8. It is not possible to fit all PL peaks of this measured spectra, with keeping the values for the fitting parameters close to the values obtained for the previous fit, see table 4.4.2. Although the regularity and the relative position of the peaks resulting from this fitting method are in good agreement between the two different spectra. For a complete overview of the fit for

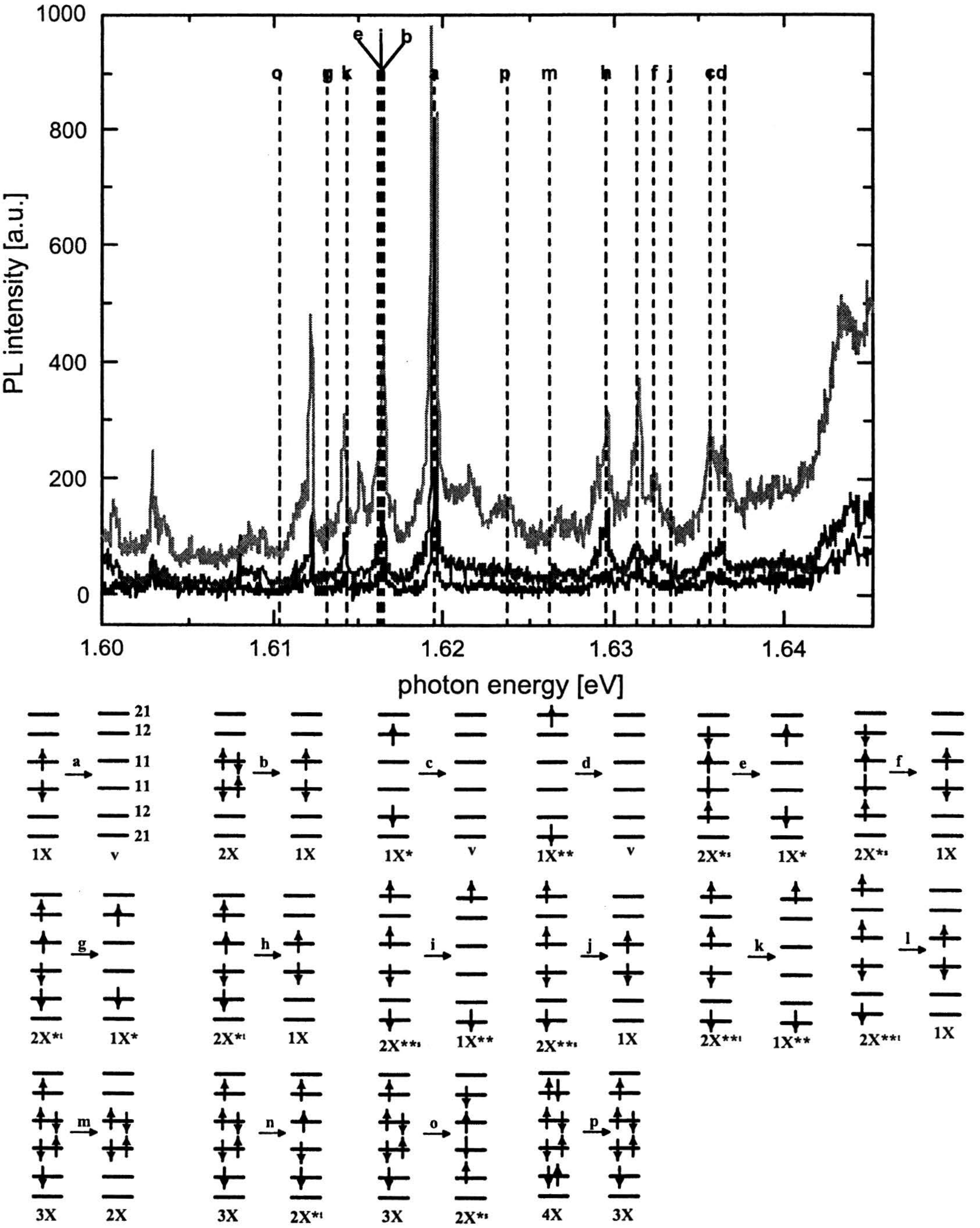

Figure 4.10: *Micro-PL spectra, excited with the Ti;sapphire laser in mode lock at 746 nm, measured at identical positions on the sample taken at 160, 320 and 480 W/cm*^{2}. *The various transitions from the three lowest energy levels are shown corresponding to the labels in Table 4.1.*

Table 4.3: *The extracted values for the various interaction terms of the two different fitting methods for Fig. 4.5. The values shown are in meV.*

interaction term	incomplete carrier relaxation	incomplete spin relaxation
$V_c^{11/11}$	-2.9	-2.9
$V_c^{11/12}$	-3.3	1.1
$V_c^{11/21}$	-3.1	1.0
$V_c^{12/12}$	-2.5	-2.9
$V_x^{11/12}$	-2.9	-5.3
$V_x^{11/21}$	-2.0	-6.3

this spectra see the appendix. The same can be done for the incomplete spin relaxation method, leading to the fit displayed in Fig. 4.11.

The quality of this fit is again rather high, with comparable values of fit of the previous spectra, see table 4.4.2. Note that the features at low photon energy (± 1.60 eV) can not be explained by either of the two fitting methods. A more extensive fit is given in the appendix. For low excitation density however, the excited single exciton recombinations in Fig. 4.5 are not that pronounced as in Fig. 4.3. This could indicate an enhanced carrier relaxation compared with the previous spectra.

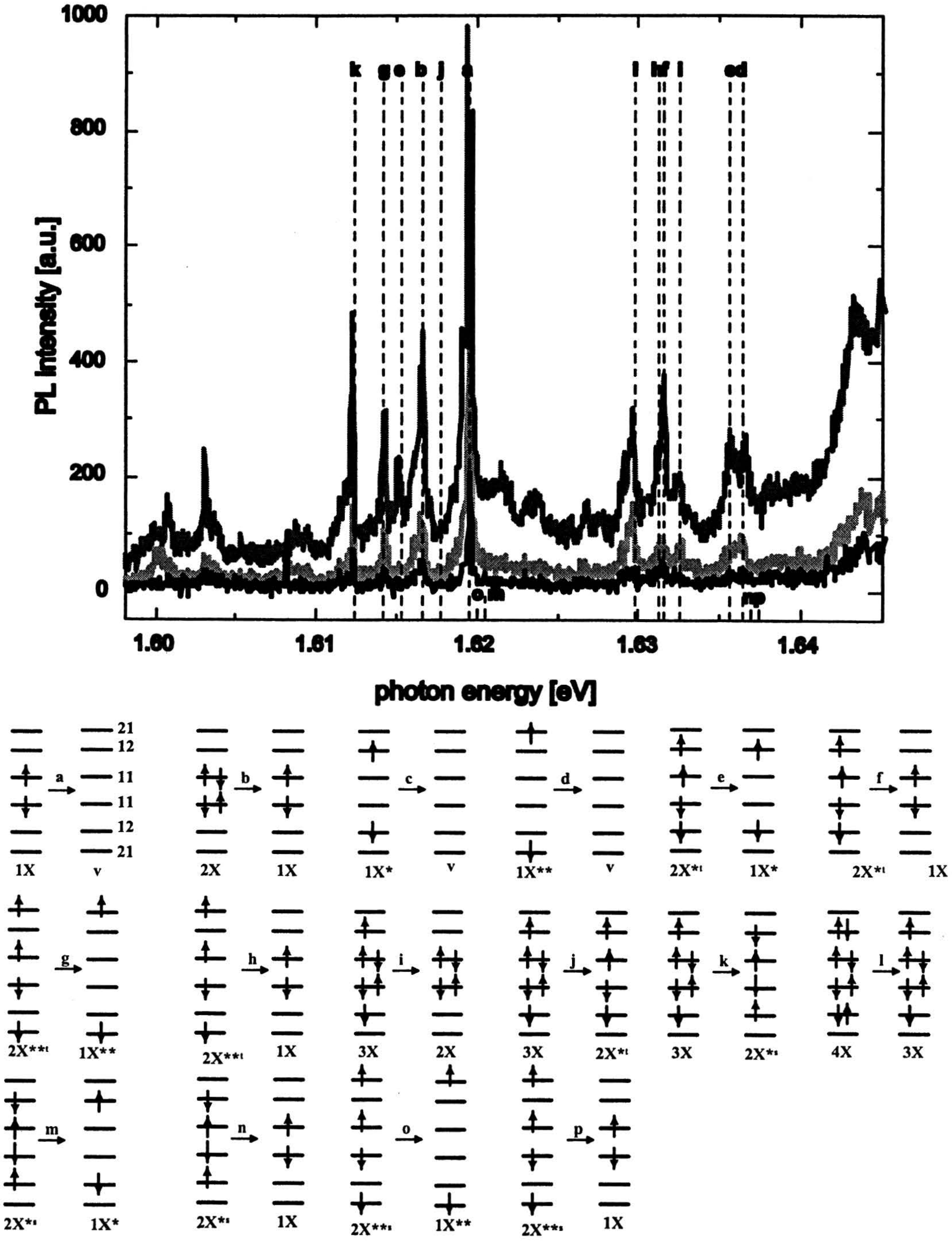

Figure 4.11: *Micro-PL spectra, excited with the Ti:sapphire laser in mode lock at 746 nm, measured at identical positions on the sample taken at 160, 320 and 480 W/cm^2. The various transitions from the three lowest energy levels are shown corresponding to the labels in Table 4.1.*

4.5 Discussion of the fitting methods

Taking into account up to four excitons and the lowest three energy levels of QDs, two Hartree-Fock based fitting procedures are used to fit the measured spectra. The incomplete carrier relaxation method is depending on the presence of a phonon bottleneck in the QDs. In contrast to SAQDs, our QDs are strictly strain free, circumventing strain induced polarisation effects within the dot [27], which might lead to the existence of a phonon bottleneck. Especially the first spectrum 4.8 can be fitted accurately by the ICR method. This method correctly predicts the position of the 3X → 2X recombination, which is becoming visible at higher excitation densities. At such excitation density, also the other possible recombination from 3X to excited 2X states should become visible. At even higher excitation density the 4X → 3X will be visible as well. The value of the additional free fitting parameter for identifying the 4X → 3X transition is in good agreement with other values, which makes the position of that transition plausible. Figures Ba and Bb in the appendix displays that the PL lines appear in two groups. One group consists of PL lines originating from recombinations of an exciton in the ground state (s-shell recombinations), the other group consists of PL lines originating from recombinations of an exciton from either the (12) or (21) energy level (p-shell recombinations). The highest possible recombination energy from the s-shell is the single exciton recombination, all other exciton recombinations from the s-shell will have additional Coulomb or exchange term lowering the recombination energy. The highest p-shell recombination is $1X^{**}$ → to vacuum and the lowest possible p-shell recombinations considering up to four excitons in the incomplete carrier relaxation is the 4X → 3X recombination. These two values set an energy range in which all possible p-shell recombination will recombine. In the case of incomplete spin relaxation this is slightly different, because also positive terms come into play. However almost all p-shell recombinations for both fitting methods have an higher recombination energy than the single exciton recombination energy. From the extensive fits in the appendix it can be seen that the predicted closely packed PL lines coincide with measured PL peaks. Comparing the incomplete carrier relaxation with the incomplete spin relaxation for spectra measured in Fig. 4.3 some significant differences are noticeable. For the incomplete spin relaxation the transitions from 3 or 4 exciton complexes are already visible at relative low excitation densities compared to the incomplete carrier relaxation. The incomplete spin relaxation method predicts identical recombination energies for transitions for several recombination transitions consisting out of 3 or 4 excitons. Hence for higher excitation densities the probability to observe recombination from 3 or 4 exciton complexes becomes higher, due to overlapping transitions from different configuration with identical recombination energy. The increase in intensity of 3 or 4 exciton recombination for increasing excitation density recombination could thus be explained. Concerning the global positions of the s- and p-shell recombinations of the different fitting methods ISR would have a slight preference. The predicted lines in the ISR-method are in better overlap with the measured PL peaks and also the most pronounced measured PL peaks lie within the predicted energy range of the p-shell of the ISR-method. The approximate position of the peaks is directly related to values for the fitting parameters. The values for the different Coulomb energies are expected to be close to zero either positive or negative, which is for both fits in good agreement. The exchange energies of the ISR-method are closer to the exchange energies theoretically calculated (- 7.0 meV) for a QD with impenetrable walls. In the practice the exchange energies are expected to be lower which would give the ISR-method the preference. However, the transition 3X → $2X^{*t}$ (line 'k' in Fig. 4.9) does not overlap with a measured peak in the incomplete spin relaxation fitting method. Although the 3X → $2X^{*t}$ recombination is quite probable to occur and is thus likely to be measured. The predicted position of the 3X → $2X^{*t}$ recombination does not coincide with a measured peak, but lies in a shoulder in between the exciton and biexciton recombination lines. These considerations would favor the incomplete carrier relaxation above the incomplete spin relaxation fitting method for the spectra of Fig. 4.3.

An analogue comparison can be made for the two fitting methods considering the spectra of Fig. 4.5b. The ICR-method has less overlap with the measured spectra. It is found to be difficult to fit the measured PL peaks with the ICR-method keeping the fitting values close to the fitting values of the previous spectra. An other possibility is to choose the position of the excited single excitons differently, but even then it was difficult to improve the quality of the fit. The Coulomb energies are once again in good agreement with the expected values and also with the values of the previous fit. The exchange energies however are even lower than in the previous fit, leading to a larger discrepancy between the theoretical calculated value and the fitted value. Looking into detail to the ISR-method there is again no overlap observed between the 3X → $2X^{*t}$ and a measured PL peak. However, this is the only relevant transition which can not be fitted by this method and all other predicted lines are in good agreement with the measured spectrum. Especially the predicted p-shell recombinations are in close overlap with observed PL peaks as can be seen in Fig. B of the appendix. Even for higher excitation energies no significant additional peaks become visible, which is also not predicted by the ISR-method. The ICR-method predicts peaks in that region where no significant peaks appear at higher excitation densities. Noticeable also is the conformity of the fitted values for the ISR-method not only with the previous spectrum, but also with the theoretical predicted values. Detailed analysis of the spectrum of 4.5b favors the ISR-method instead of the ICR-method. Another contrast between the two spectra is the intensity of the excited single exciton peaks, as mentioned before. The lower intensity of the excited single exciton peaks in Fig. 4.5b could indicate an enhanced carrier relaxation with respect to the measured spectra of Fig. 4.3. Apparently, the behavior of the carriers are locally, on the length scale up to several micrometers, homogeneous but macroscopic their behavior can change. Therefore it is possible that the carrier relaxation rates within the QDs, determining the amount of excited-state PL, can vary with macroscopic position.

4.6 General Discussion

Assuming fast hole relaxation, as suggested in literature [12], could perhaps lead to an improved fit of the measured PL spectra. The energy levels of holes are much closer to each other than the electron energy levels. Due to the lifetime broadening ($\hbar/t_{life}$) of the hole energy levels the closely spaced hole energy levels can overlap. This results in a continuum of allowed hole energy levels and hence the hole relaxation will be fast. Fast relaxation of holes, captured with zero total spin and slower electron relaxation, would imply that only electrons can occupy excited energy levels and that the optical polarisation is depending on the electron spin. Preliminary results of polarisation dependent measurements however, do not indicate a different polarisation for different PL peaks. In this situation, not only a new manner of filling the QD has to be considered, but also new exciton recombinations appear. Figure 4.12a show a number of possible (multi-)exciton configurations. The selection rules for QDs, conservation of $n_i^e = n_i^h$, determine which transitions are allowed or not, see Fig. 4.12b and 4.12c. The transitions shown in Fig. 4.12b assuming fast hole relaxation are very likely to occur and obey the QD selection rules in contrast to the transition in Fig. 4.12c. It is also shown that the electron spin will determine the polarisation of the photon.

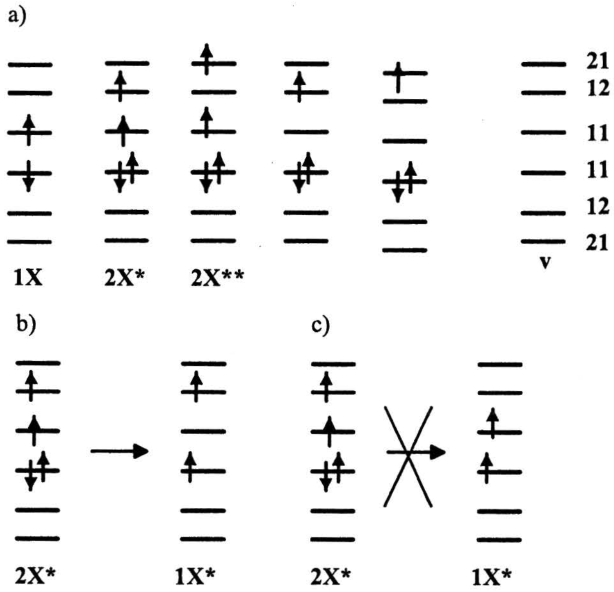

Figure 4.12: *a) Various possible carrier configuration assuming fast hole relaxations. Charge neutrality is maintained by electrons occupying higher energy levels. Possible recombination assuming fast hole relaxation are shown in b) and c). The transition of b) obeys the QD selection rules in contrast to transition of c).*

It can be seen that by assuming fast hole relaxation additional fitting parameters such as shown in the PL energy are required.

$$E_{PL} = E_e^{11} + E_h^{11} - 2V_{eh}^{11/11} - V_{eh}^{11/12} + V_{ee}^{11/12} + V_{hh}^{11/11}.$$

All Coulomb and exchange terms now come into play, where in the case of identical relaxation times for electrons and holes, the Coulomb terms often appeared in pairs. These pairs denoted as $V_c^{11/12} = V_{ee}^{11/12} + V_{hh}^{11/12} - 2V_{eh}^{11/12}$, reduced the number of fitting parameters. Therefore more PL lines need to be chosen in the case of fast hole relaxation in order to be able to assign values to the different Coulomb and exchange interactions. The possible exciton configurations, considered in Fig. 4.12a assuming fast hole relaxation could result in an unequal number of electrons and holes in the QD indicating a charged QD. Because we only consider the three lowest energy levels an unequal number of electrons and holes could appear. However, due to the slower electron relaxation, electrons will occupy higher energy levels, which are not shown here, maintaining charge neutrality in the QD. As already discussed previously, charged QDs are not likely to occur in our case.
According to the two fitting methods it seems inevitable to assume incomplete carrier relaxation or a phonon bottleneck, but is this reasonable? In the vast majority of measurements concerning carrier relaxation no phonon bottleneck has been observed, especially not in SAQDs. Minneart *et al.* have reported that the phonon-assisted PL is due to enhanced Frölich interactions between strain-induced polarised excitons in SAQDs and LO phonons [27]. In SAQDs a net charge distributions resulting in a dipole is expected [35] to be present due to strain effects, see Fig. 4.13.

The growth of III - V materials results in a polar environment because of the different charges of group III and group V elements. The polarised exciton interacts with the polar lattice atoms, which gives rise to an enhancement of the Frölich interaction. Therefore a strong coupling between the lattice and the confined excitons is present and relaxation by emitting LO phonons is more effective. In our strain-free QDs, we do not expect a polarised exciton giving rise to an enhanced Fröhlich interaction. Consequently a phonon bottleneck might be present in our "ideal" QDs, explaining the observed incomplete carrier relaxation.

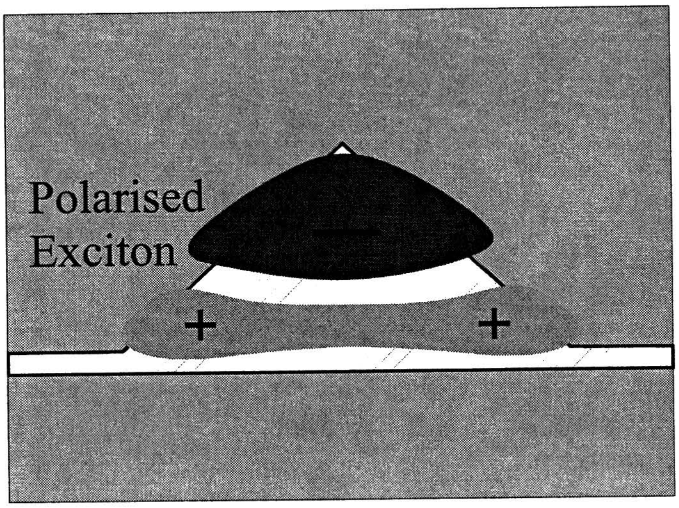

Figure 4.13: *Artist impression of the charge distribution in SAQDs.*

Chapter 5

Conclusions and Recommendations

In this work, we studied μ-PL on QDs and performed detailed analysis of the obtained spectra, in order to get a better insight in the carrier dynamics and fundamental physics of QDs. Especially the strain freeness of our QDs is a key element for the study of the intrinsic properties of QDs. Conclusions can be drawn regarding the homogeneity of the QD sample itself, for the interpretation of the μ-PL spectrum and also the carrier relaxation mechanism. Furthermore some recommendations for future work are given.

5.1 QD homogeneity

Throughout this report, the assumption is made that we are dealing with homogeneous QD-arrays on length scales up to several micrometers. A number of strong indications for the local homogeneity of the QDs in the arrays have been obtained to justify this assumption. (i) Upon scanning the excitation spot along the QD-array, the abrupt and simultaneous appearance and disappearance of successive multi-excitonic features with very sharp peaks (< 0.2 meV) is observed. (ii) The QD emission peaks show a small asymmetric broadening, as already reported by Nötzel [4], which indicates small size fluctuations between the homogeneous QDs. (iii) The excitation density depending measurements show the arising of new peaks with increasing intensity also indicating a multi-excitonic spectrum. (iv) After analysis of many measured PL spectra, the spectra do not show randomly distributed peaks along the energy axis; the positions of the different peaks are strongly correlated. (v) Our exciton lifetime measurements using TCSPC and pulsed excitation show that only the ground state exciton has a delayed risetime [11, 32] at higher excitation density. Such a delayed risetime is typical for ground state exciton since the ground state exciton recombination line becomes visible after recombination of all other (multi-)exciton complexes.

Taking into account these indications, we thus can interpret the μ-PL spectra as multi-excitonic spectra from locally homogeneous QD-arrays. On macroscopic distances along the QD-array however, the μ-PL spectra can strongly vary, indicating that the QD dimensions and excited state degeneracy, determined by the differences in the QD dimension along the $[01\bar{1}]$ and $[\bar{2}33]$ vary substantially. As mentioned before, the carrier relaxation rates within the QDs, determining the amount of excited PL, can vary significantly with macroscopic position.

5.2 Photoluminescence on the QD sample

The obtained μ-PL spectra show excitonic and multi-exciton recombination, including excited exciton and excited biexciton recombinations. Focussing on the multi-excitonic characteristics of the spectra, we have treated the QD confinement levels with a simple particle-in-a-box model. Such a simple model is valid since the band offsets of our GaAs/$\mathrm{Al_{0.7}Ga_{0.3}As}$ QDs are comparatively large. Then it is allowed to use this model to make an approximation for the QD dimensions with the help of excited exciton recombinations. Subsequently, the Coulomb and exchange interactions that arise between the carriers occupying the energy levels of a QD by applying the Hartree Fock (HF) approximation are taken into account. The HF terms are used as corrections on the single particle energies. The exciton and excited exciton recombinations are used to fit E_{1X}, E_{1X^*} and $E_{1X^{**}}$ which are correlated with the QD dimensions. The 2X → 1X recombination is used to fit the biexciton binding energy $V_c^{11/11}$. The extracted QD dimensions are in good agreement with AFM measurements [4]. The biexciton binding energy is also close to reported biexciton binding energy values reported in literature [30, 31].

Once these four lines in the spectrum are fixed, 11 other peaks can be fitted accurately using four additional fitting parameters; $V_c^{11/12}$, $V_x^{11/12}$, $V_c^{11/21}$ and $V_x^{11/21}$. Two fitting methods based on two different principles, incomplete carrier relaxation (ICR) and incomplete spin relaxation (ISR), display a quite good agreement with the measured spectra. The two different fitting methods result in slightly different values for the fitting parameters. The obtained values vary slightly with the theoretical predicted values, but are in good agreement with previously reported values. Our simple particle-in-a-box model predicts a zero biexciton binding energy as well as for $V_c^{11/12}$ and $V_c^{11/21}$. Since these terms consists of four Coulomb terms, the exact values of the Coulomb energy corrections are sensitive to detailed shape and charge distributions within the QD. In practice, depending on whether the electron-electron and hole-hole repulsion is weaker or larger than the electron-hole attraction either positive or negative values result for the various Coulomb terms. For the exchange interactions good agreement with the theoretical calculated value (-7.0 meV) is obtained. The slight variations is again caused by the simplicity of our model, which is based on ideal QDs which have impenetrable walls. In practice, the wavefunctions of the carriers will penetrate into the barrier and hence the exchange energy will decrease due to the decrease of the wavefunctions from different energy levels. Only the 4X→ 3X recombination requires one more additional free parameter $V_c^{12/12}$. The obtained values for this parameter are in close agreement with the other Coulomb terms which makes the fit plausible.

Our assignment of the QD spectrum critically depends on the carrier occupation of the QD energy levels. The straightforward assumption of complete carrier relaxation before carrier recombination fails to explain some pronounced PL lines, which emerge already at low excitation density. PL peaks can be assigned by allowing excited single exciton and excited biexciton recombinations, pointing toward an incomplete carrier relaxation or a phonon bottleneck. Assuming fast carrier relaxation and slow spin relaxation, excited spin triplet states are unable to relax to the ground state without spin relaxation. In this incomplete spin relaxation model PL peaks can also be assigned accurately. Note that also for incomplete spin relaxation, slowed down carrier relaxation is assumed. It is remarkable however, that the best fits are obtained by including excited single- and biexciton recombinations indicating a phonon bottleneck, within this strain free QD sample. Substantial variations in the dimensions, symmetry and carrier relaxation rates with macroscopic position along the QD-arrays lead to different PL characteristics of the measured sample with macroscopic position. It has been shown by means of the two different fitting methods that the measured PL peaks can be predicted quite well. In SAQDs the absence of a phonon bottleneck is attributed to strain induced polarised excitons [27]. We believe that such an incomplete carrier relaxation within our strain free QD-arrays is the only way to explain the very rich and strongly correlated μ-PL spectra observed in this sample. Although an unambiguous fitting method is not obtained, we do have two fitting methods which are able to predict the regularity of the measured PL peaks quite well.

5.3 Recommendations

The goal to improve the understanding of the fundamental physics of QDs, leads to single dot spectroscopy. Although considering a homogeneous QD-array, we are still studying an ensemble of QDs. To achieve single QD spectroscopy, a combination of the QD growth mechanism used for our sample and masking or etching the sample in order to excite only a single QD could be used.

Additional measurements could be carried out to improve the insight in the QD properties such as polarisation dependent measurements, but also polarisation dependent excitation. Carefully performed polarising excitation and/or polarisation dependent measurements could give indications for possible spin alignment of the carriers, which can give additional information for currently existing models describing the carrier dynamics in QDs. Time resolved measurements are required to get a better insight in the relevant time scales of the different mechanisms. A combination of polarising excitation and time resolved measurement can lead to new insights in the physics of the QDs as well. Also additional PLE or RPL can come up with new information.

Furthermore, the existing model can be extended for example assuming fast hole relaxation. Assuming fast hole relaxation, carrier configurations that vary from the currently used configurations can occur and recombine. These new configurations,with different Coulomb and exchange terms might give an improved fit to the measured spectra.

Bibliography

[1] M. Colocci, F. Bogani, L. Carreresi, R. Mattolini, A. Bosacchi, S. Franchi, P. Frigeri, M. Rosa-Chlot and S. Taddei, Appl. Phys. Lett. **70**, 3140 (1997)

[2] D.M. Bruls, P.M. Koenraad and J.H. Wolter, *to be published.*

[3] K. Hinzer, P. Hawrylak, M. Korkusinski, s. Fafard, M. Bayer, O. Stern, A. Gorbunov and A. Forchel, Phys. Rev. B **63**, 075314 (2001)

[4] R. Nötzel, Z. Niu, M. Ramsteiner, H.P. Schönherr. A. Tranpert. L. Däweritz and K.H. Ploog, Nature **56**, 392 (1998)

[5] K. Brunner, G Abstreiter,G. Böhm, G. Tränkle and G. Weimann, Appl. Phys. Lett. **64**, 3320 (1994)

[6] K. Brunner, G. Abstreiter, G. Böhm, G. Tränkle and G. Weimann, Phys. Rev. Lett. **73**, 1138 (1994)

[7] H. Kamada, H. Ando, J. Temmyo and T. Tamamura, Phys. Rev. B **58**, 16243 (1998)

[8] E. Dekel, D. Gershoni, E. Ehrenfreund, D. Spektor, J.M. Garcia and P.M. Petroff, Phys. Rev. Lett **80**, 4991 (1998)

[9] A. Barenco and M.A. Dupertuis, Phys. Rev. B **52**, 2766 (1995)

[10] P. Hawrylak, Phys. Rev. B **60**, 5597 (1999)

[11] E. Dekel, D. Gershoni, E. Ehrenfreud, J.M. Garcia and P.M. Petroff, Phys. Rev. B **61**, 11009 (2000)

[12] V.K. Kalevich, M. Paillard, K.V. Kavokin, X. Marie, A.R. Kovsh, T. Amand. A.E. Zhukov. Yu.G. Musikhin, V.M. Ustinov, E. Vanelle and B.P. Zakharchenya, Phys. Rev. B **64**, 45309 (2001)

[13] Al.L. Éfros and A.L. Éfros, Sov. Phys. Semicond. **16**, 772 (1982)

[14] L. Jacak, P. Hawrylak and A. Wójs, *Quantum Dots* (Springer-Verlag, Berlin, 1998)

[15] J. E. House, *Fundamentals of Quantum Mechanics* (Academic Press, New York, 1998)

[16] J.P. Dahl, *Introduction to the quantum world of atoms and molecules* (World Scientific, Singapore, 2001)

[17] M. Bayer, A. Forchel, P. Hawrylak, S. Fafard and G. Narvaez, Phys. stat. sol. (b), **224**, 331 (2001)

[18] M. Bayer, O. Stern, P. Hawrylak, S. Fafard and A. Forchel, Nature **405**, 923, (2000)

[19] U. Woggon, *Optical Properties of Semiconductor Quantum Dots* (Springer, Berlin, 1997)

[20] M.Bayer, A. Kuther, A. Forchel, A. Gorbunov, V.B. Timofeev, F. Schäfer, J.P. Reithmaier, T.L. Reinecke and S.N. Walck, Phys. Rev. Lett. **82**, 85 (2000)

[21] P. Hawrylak, G.A. Narvaez, M. Bayer and A. Forchel, Phys. Rev. Lett. **85**, 389 (2000)

[22] T.S. Sosnowski, T.B. Norris, H. Jiang, J. Singh, K. Kamath and P. Bhattacharya, Phys. Rev. B **57** 9423 (1998)

[23] R. Heitz, M. Veit, N.N. Ledentsov, A. Hoffmann, D. Bimberg, V.M. Ustinov, P.S. Kop'ev and Zh. I. Alferov, Phys. Rev. B **56**, 10435 (1997)

[24] H. Benisty, C.M. Sotomayor-Torrès and C. Weisbuch, Phys. Rev. B **44**, 10945 (1991)

[25] U. Bockelmann and T. Egeler, Phys. Rev. B **46**, 15574 (1992)

[26] Al.L. Efros. V.A. Kharchenko and M. Rosen, Solid State Commun. **93**, 281 (1995)

[27] A.W.E. Minnaert, A.Y. Silov, W. v.d. Vleuten, J.E.M. Haverkort, J.H. Wolter, Phys. Rev. B, **63**, 075303 (2001)

[28] K. Brunner,U. Bockelmann,G. Abstreiter,M. Walther,G. Böhm, G. Tränkle, G. Weimann, Phys. Rev. Lett. **69**, 3216 (1992)

[29] R. Nötzel, J. Menniger, M. Ramsteiner, A. Ruiz, H.P. Schnherr, and K. H. Ploog, Appl. Phys. Lett. **68**, 1132 (1996)

[30] M. Bayer, T. Gutbrod, A. Forchel, V.D. Kulakovskii, A. Gorbunov, M. Michel, R. Steffen and K.H. Wang, Phys. Rev. B **58**, 4740 (1998)

[31] L. Landin, M.E. Pistol, C Pryor, M Persson, L. Samuelson and M. Miller, Phys. Rev. B **60**, 16640 (1999)

[32] G. Bacher, R. Weigand, J. Seufert, N.A. Gippius, V.D. Kulakovskii, A. Forchel, K. Leonardi and D. Hommel, Phys. Stat. Sol. (b) **221**, 25 (2000)

[33] H. Gotoh, H Ando, H Kamada, A Chavez-Pirson and J. Temmyo, Appl. Phys. Lett. **72**, 1341 (1998)

[34] A.V. Khaetskii and Y.V. Nazarov, Phys. Rev. B **61**, 12639 (2000)

[35] M.A. Cusack,P.R. Riboon and M. Jaros, Phys. Rev. Lett. **54**, 2300 (1996)

Appendix A

Estimation of the QD dimensions

The QD dimensions can be estimated by varying the three dimensions such that the recombination energy of possible transitions coincide with the measured energies. Three PL energies are required to determine the three independent parameters (a, b and c) to obtain the QD dimensions. The single (excited) excitons recombinations are used to determine the QD dimensions due to minimum number of to be calculated terms. Using ??eq:1X) the exciton recombination energy can be calculated by the confinement energies and the Coulomb interaction of the electron-hole pair added by the band gap energy of 1.519 eV. The confinement energies are calculated by equation (2.12) and the Coulomb interaction energy for the exciton by:

$$\int_0^a \int_0^b \int_0^c \phi_{11}^{e*} \phi_{11}^{h*} V_c \phi_{11}^{e} \phi_{11}^{h} dx dy dz, \tag{A.1}$$

where V_c is defined by (2.16). The calculated recombination energy is calculated and subsequently checked with the measured values. This procedure is repeated until the calculated recombination energies have a good overlap with the measured values. This procedure is done for the three single (excited) exciton recombination energies at the same time, resulting in values as shown in table A.1.

The single (excited) recombination energies are 1.6319, 1.646 and 1.6479 and 1.6197, 1.6356 and 1.6364 eV respectively for the two different dots. The eventual QD dimensions are 36.2 x 38.9 x 7.40 and 36.5 x 35.5 x 7.84 nm^3 for the two dots respectively, which is in reasonable agreement with AFM measurements.

Table A.1: *Calculated values for the ground state and single excited exciton confinement energies as well as the Coulomb terms to get an estimation for the QD dimensions. Adding these terms results in the recombination energies of the measured spectra.*

Energy term	Fig. 4.3 [meV]	Fig. 4.5 [meV]
$E_e^{11} + E_h^{11}$	125.4	113.5
$E_e^{12} + E_h^{12}$	138.0	127.8
$E_e^{21} + E_h^{21}$	139.9	128.6
$V_{c,eh}^{11/11}$	12.5	12.8
$V_{c,eh}^{12/12}$	11.0	11.2
$V_{c,eh}^{21/21}$	11.0	11.2

Appendix B

Extensive fits for the measured spectra

All possible configurations, as shown in Fig. B.1, which are possible with up to four excitons and three energy levels, can have a contributions in the PL spectra. In order to be able to fit the measured spectra accurately, the corresponding recombination energies of the possible transitions have to be taken into account. The relevant Coulomb and exchange interactions, displayed in Fig. B.2 and B.4, have to be varied in order to obtain the best overlap with the measured spectra. Each transition gives rise to a recombination line in the PL spectra. Figures B.3 and B.5 show that the approximate positions of the predicted PL energies for the two fitting methods have a good agreement with the measured spectra. Also the s- and p-shell recombination are distinguishable in these extensive fits. The highest possible recombination energy from the s-shell is the single exciton recombination, all other exciton recombinations from the s-shell will have additional Coulomb or exchange term lowering the recombination energy. The highest p-shell recombination is $1X^{**} \rightarrow$ vacuum and the lowest possible p-shell recombinations considering up to four excitons in the incomplete carrier relaxation is the $4X \rightarrow 3X$ recombination. These two values set an energy range in which all possible p-shell recombination will recombine. In the case of incomplete spin relaxation this is slightly different, because also positive terms come into play. However almost all p-shell recombinations for both fitting methods have an higher recombination energy than the single exciton recombination energy.

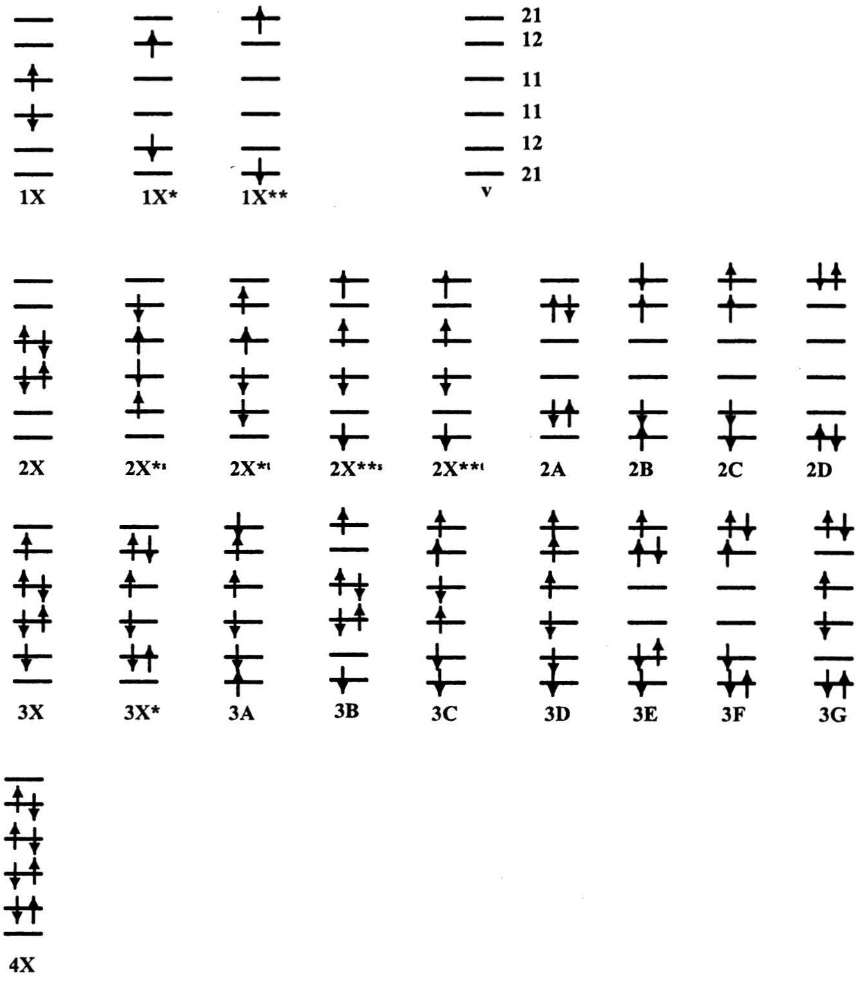

Figure B.1: *Various multi-excitonic configurations taking into account only the lowest three energy levels. Vertical arrows indicate the electron and hole spin states. Superscript 's' ant 't' indicate singlet and triplet configurations respectively. The labels of the various configurations correspond with the labels in Fig. B.3 and B.5.*

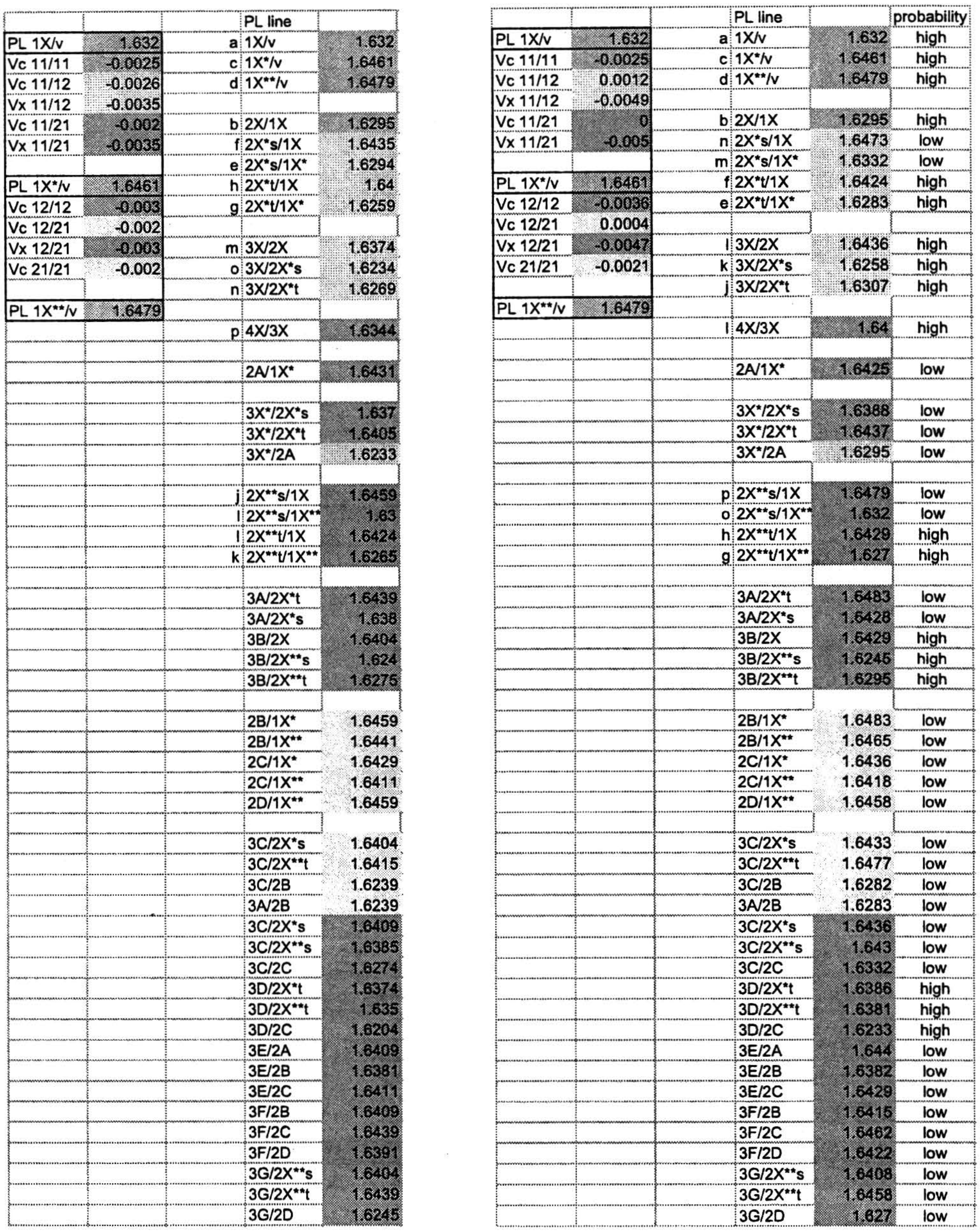

Incomplete carrier relaxation

			PL line	
PL 1X/v	1.632	a	1X/v	1.632
Vc 11/11	-0.0025	c	1X*/v	1.6461
Vc 11/12	-0.0026	d	1X**/v	1.6479
Vx 11/12	-0.0035			
Vc 11/21	-0.002	b	2X/1X	1.6295
Vx 11/21	-0.0035	f	2X*s/1X	1.6435
		e	2X*s/1X*	1.6294
PL 1X*/v	1.6461	h	2X*t/1X	1.64
Vc 12/12	-0.003	g	2X*t/1X*	1.6259
Vc 12/21	-0.002			
Vx 12/21	-0.003	m	3X/2X	1.6374
Vc 21/21	-0.002	o	3X/2X*s	1.6234
		n	3X/2X*t	1.6269
PL 1X**/v	1.6479			
		p	4X/3X	1.6344
			2A/1X*	1.6431
			3X*/2X*s	1.637
			3X*/2X*t	1.6405
			3X*/2A	1.6233
		j	2X**s/1X	1.6459
		l	2X**s/1X**	1.63
		l	2X**t/1X	1.6424
		k	2X**t/1X**	1.6265
			3A/2X*t	1.6439
			3A/2X*s	1.638
			3B/2X	1.6404
			3B/2X**s	1.624
			3B/2X**t	1.6275
			2B/1X*	1.6459
			2B/1X**	1.6441
			2C/1X*	1.6429
			2C/1X**	1.6411
			2D/1X**	1.6459
			3C/2X*s	1.6404
			3C/2X**t	1.6415
			3C/2B	1.6239
			3A/2B	1.6239
			3C/2X*s	1.6409
			3C/2X**s	1.6385
			3C/2C	1.6274
			3D/2X*t	1.6374
			3D/2X**t	1.635
			3D/2C	1.6204
			3E/2A	1.6409
			3E/2B	1.6381
			3E/2C	1.6411
			3F/2B	1.6409
			3F/2C	1.6439
			3F/2D	1.6391
			3G/2X**s	1.6404
			3G/2X**t	1.6439
			3G/2D	1.6245

Incomplete spin relaxation

			PL line		probability
PL 1X/v	1.632	a	1X/v	1.632	high
Vc 11/11	-0.0025	c	1X*/v	1.6461	high
Vc 11/12	0.0012	d	1X**/v	1.6479	high
Vx 11/12	-0.0049				
Vc 11/21	0	b	2X/1X	1.6295	high
Vx 11/21	-0.005	n	2X*s/1X	1.6473	low
		m	2X*s/1X*	1.6332	low
PL 1X*/v	1.6461	f	2X*t/1X	1.6424	high
Vc 12/12	-0.0036	e	2X*t/1X*	1.6283	high
Vc 12/21	0.0004				
Vx 12/21	-0.0047	l	3X/2X	1.6436	high
Vc 21/21	-0.0021	k	3X/2X*s	1.6258	high
		j	3X/2X*t	1.6307	high
PL 1X**/v	1.6479				
		l	4X/3X	1.64	high
			2A/1X*	1.6425	low
			3X*/2X*s	1.6388	low
			3X*/2X*t	1.6437	low
			3X*/2A	1.6295	low
		p	2X**s/1X	1.6479	low
		o	2X**s/1X**	1.632	low
		h	2X**t/1X	1.6429	high
		g	2X**t/1X**	1.627	high
			3A/2X*t	1.6483	low
			3A/2X*s	1.6428	low
			3B/2X	1.6429	high
			3B/2X**s	1.6245	high
			3B/2X**t	1.6295	high
			2B/1X*	1.6483	low
			2B/1X**	1.6465	low
			2C/1X*	1.6436	low
			2C/1X**	1.6418	low
			2D/1X**	1.6458	low
			3C/2X*s	1.6433	low
			3C/2X**t	1.6477	low
			3C/2B	1.6282	low
			3A/2B	1.6283	low
			3C/2X*s	1.6436	low
			3C/2X**s	1.643	low
			3C/2C	1.6332	low
			3D/2X*t	1.6386	high
			3D/2X**t	1.6381	high
			3D/2C	1.6233	high
			3E/2A	1.644	low
			3E/2B	1.6382	low
			3E/2C	1.6429	low
			3F/2B	1.6415	low
			3F/2C	1.6462	low
			3F/2D	1.6422	low
			3G/2X**s	1.6408	low
			3G/2X**t	1.6458	low
			3G/2D	1.627	low

Figure B.2: *Possible transitions considering up to four excitons and three energy levels for the spectra measured in Fig. 4.3. The labels 'a' through 'p' correspond with transitions from table 4.1. The expected probability in case of the ISR-method is also displayed.*

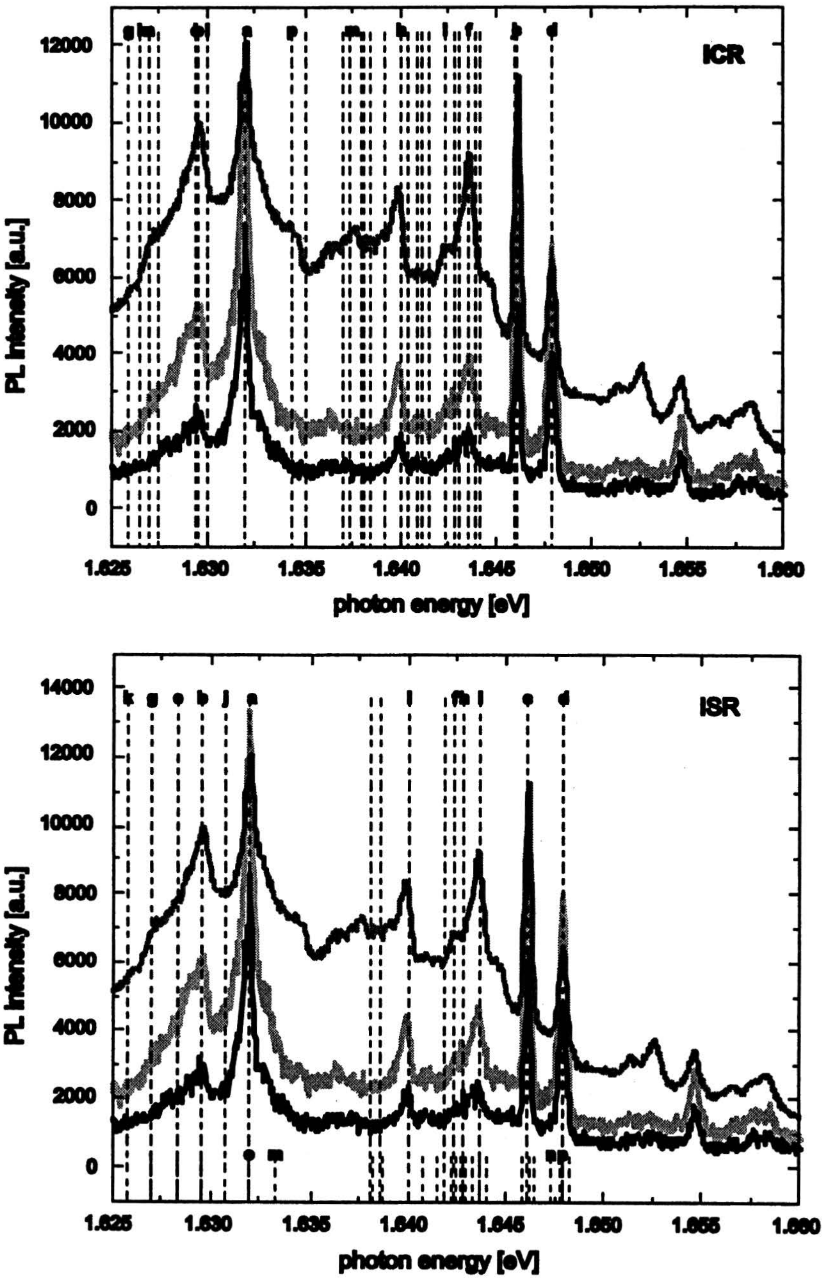

Figure B.3: *Extensive fit of all possible transitions listed in Fig. B.2 for the ICR- and ISR-method.*

Incomplete carrier relaxation

			PL line	
PL 1X/v	1.6194	a	1X/v	1.6194
Vc 11/11	-0.0029	c	1X*/v	1.6357
Vc 11/12	-0.0033	d	1X**/v	1.6364
Vx 11/12	-0.0029			
Vc 11/21	-0.0031	b	2X/1X	1.6165
Vx 11/21	-0.002	f	2X*s/1X	1.6324
		e	2X*s/1X*	1.6161
PL 1X*/v	1.6357	h	2X*t/1X	1.6295
Vc 12/12	-0.0025	g	2X*t/1X*	1.6132
Vc 12/21	-0.0022			
Vx 12/21	-0.003	m	3X/2X	1.6262
Vc 21/21	-0.0019	o	3X/2X*s	1.6103
		n	3X/2X*t	1.6132
PL 1X**/v	1.6364			
		p	4X/3X	1.6237
			2A/1X*	1.6332
			3X*/2X*s	1.627
			3X*/2X*t	1.6299
			3X*/2A	1.6099
		j	2X**s/1X	1.6333
		l	2X**s/1X**	1.6163
		l	2X**t/1X	1.6313
		k	2X**t/1X**	1.6143
			3A/2X*t	1.6311
			3A/2X*s	1.6273
			3B/2X	1.6282
			3B/2X**s	1.6114
			3B/2X**t	1.6134
			2B/1X*	1.6342
			2B/1X**	1.6335
			2C/1X*	1.6312
			2C/1X**	1.6305
			2D/1X**	1.6345
			3C/2X*s	1.6291
			3C/2X**t	1.6302
			3C/2B	1.611
			3A/2B	1.6101
			3C/2X*s	1.6281
			3C/2X**s	1.6272
			3C/2C	1.613
			3D/2X*t	1.6261
			3D/2X**t	1.6243
			3D/2C	1.6081
			3E/2A	1.629
			3E/2B	1.628
			3E/2C	1.631
			3F/2B	1.6293
			3F/2C	1.6323
			3F/2D	1.6283
			3G/2X**s	1.6294
			3G/2X**t	1.6314
			3G/2D	1.6112

Incomplete spin relaxation

			PL line		probability
PL 1X/v	1.6194	a	1X/v	1.6194	high
Vc 11/11	-0.0029	c	1X*/v	1.6357	high
Vc 11/12	0.0011	d	1X**/v	1.6364	high
Vx 11/12	-0.0053				
Vc 11/21	0.001	b	2X/1X	1.6165	high
Vx 11/21	-0.0063	n	2X*s/1X	1.6368	low
		m	2X*s/1X*	1.6205	low
PL 1X*/v	1.6357	f	2X*t/1X	1.6315	high
Vc 12/12	-0.0031	e	2X*t/1X*	1.6152	high
Vc 12/21	0.0005				
Vx 12/21	-0.0045	l	3X/2X	1.6326	high
Vc 21/21	0.008	k	3X/2X*s	1.6123	high
		j	3X/2X*t	1.6176	high
PL 1X**/v	1.6364				
		l	4X/3X	1.6295	high
			2A/1X*	1.6326	low
			3X*/2X*s	1.6284	low
			3X*/2X*t	1.6337	low
			3X*/2A	1.6163	low
		p	2X**s/1X	1.6374	low
		o	2X**s/1X**	1.6204	low
		h	2X**t/1X	1.6311	high
		g	2X**t/1X**	1.6141	high
			3A/2X*t	1.6379	low
			3A/2X*s	1.632	low
			3B/2X	1.6321	high
			3B/2X**s	1.6112	high
			3B/2X**t	1.6175	high
			2B/1X*	1.6369	low
			2B/1X**	1.6362	low
			2C/1X*	1.6324	low
			2C/1X**	1.6317	low
			2D/1X**	1.6444	low
			3C/2X*s	1.6316	low
			3C/2X**t	1.6373	low
			3C/2B	1.6152	low
			3A/2B	1.6162	low
			3C/2X*s	1.6334	low
			3C/2X**s	1.6328	low
			3C/2C	1.6215	low
			3D/2X*t	1.6271	high
			3D/2X**t	1.6275	high
			3D/2C	1.6099	high
			3E/2A	1.6329	low
			3E/2B	1.6286	low
			3E/2C	1.6331	low
			3F/2B	1.6404	low
			3F/2C	1.6449	low
			3F/2D	1.6322	low
			3G/2X**s	1.6391	low
			3G/2X**t	1.6454	low
			3G/2D	1.6151	low

Figure B.4: *Possible transitions considering up to four excitons and three energy levels for the spectra measured in Fig. 4.5b. The labels 'a' through 'p' correspond with transitions from table 4.1. The expected probability in case of the ISR-method is also displayed.*

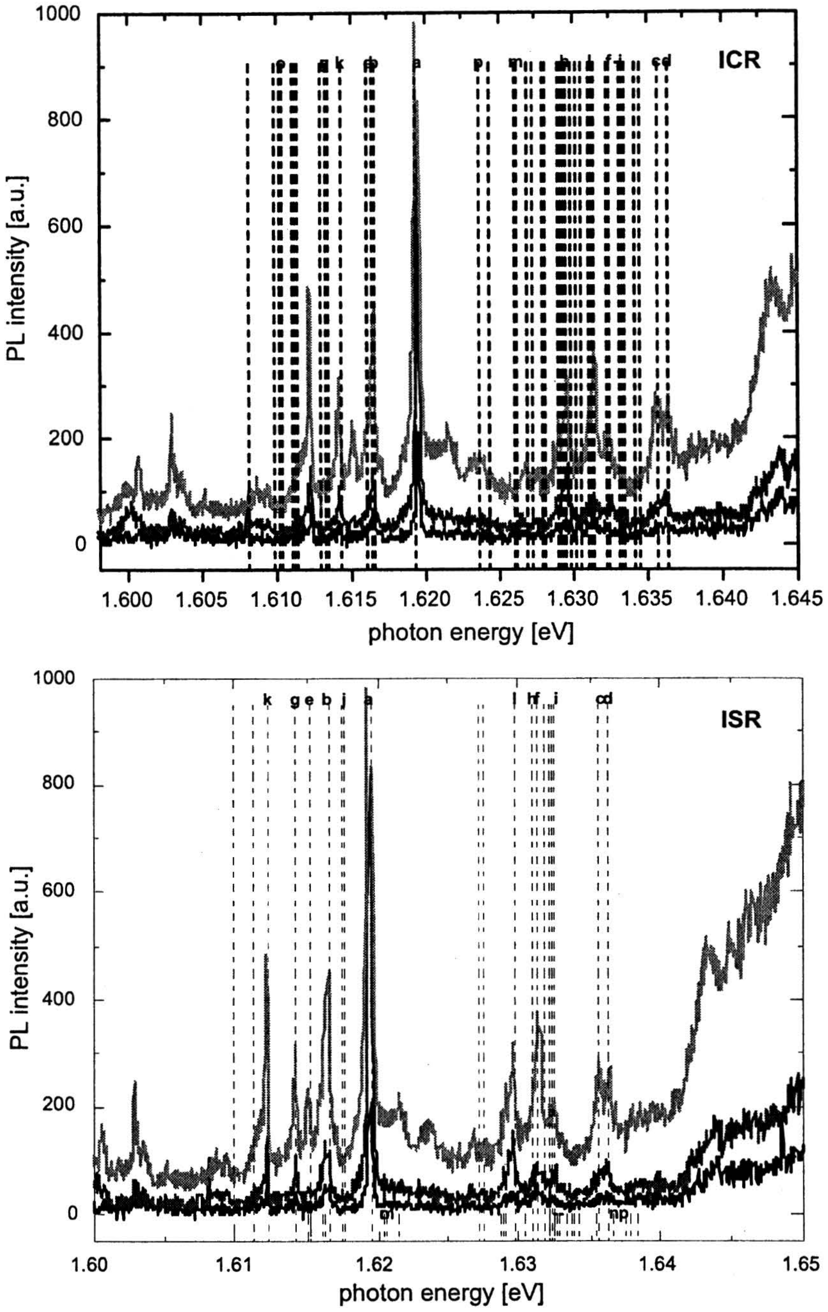

Figure B.5: *Extensive fit of all possible transitions listed in Fig. B.4 for the ICR- and ISR-method.*

Acknowledgements

Bedankjes

Uiteraard was dit werk niet gelukt zonder de hulp en ondersteuning, direct of indirect, van een aantal personen die ik hiervoor wil bedanken.
Allereerst Prof. Wolter voor de mogelijheden die hij me heeft gegeven om bij HGF te komen afstuderen, als ook de kans die hij me gaf om een buitenlandse ervaring op te doen.
Jos Haverkort voor zijn vakkundige ondersteuning als begeleider en zijn kennis op het gebied van de quantum dots. Vooral ook voor het oplossen van de laserprobleembjes.
Frank voor de dagelijkse ondersteuning en samenwerking. Vele discussies, gesprekken en brainstorm sessies hebben we gevoerd over de halfgeleiderfysica die mijn inzicht aanzienlijk hebben vergroot. Bovendien als kamergenoot hebben we over diverse zaken (o.a. welke wijn we zouden kiezen voor de volgende wijntasting) prettige gesprekken gehad.
Jos van Ruyven voor de hulp met de cryostaat en de verschillende pompen als die weer eens kuren hadden. Verder alle andere HGF-leden met wie ik het afgelopen jaar heb samengewerkt.
Mijn teamgenoten van "Bal op 't dak" voor de nodige wekelijkse in-/ontspanning tijdens de lunchpauzes op dinsdag met het zaalvoetballen.
Natuurlijk mijn ouders vooral tijdens de eerste jaren van mijn studie voor alles dat jullie voor mij hebben gedaan.
Last but not least, vooral ook Randi voor wie het niet altijd even makkelijk moet zijn geweest om met mij samen te wonen, vooral niet de laatste paar weken. Randi bedankt voor je onvoorwaardelijke steun gedurende mijn hele studie waar ik je zeer dankbaar voor ben.

Dank jullie wel